JGR Solid Earth

RESEARCH ARTICLE
10.1029/2021JB022239

Dilatancy Toughening of Shear Cracks and Implications for Slow Rupture Propagation

Nicolas Brantut[1]

[1]Department of Earth Sciences, University College London, London, UK

Key Points:

- Dilatancy strengthening leads to an increase in toughness of expanding shear cracks, which grows with increasing rupture speed
- Crack propagation can be limited by the rate of fluid recharge far behind the crack tip
- Dilatancy effect with reasonable parameter values is consistent with the dynamics of slow slip in subduction zones

Correspondence to:
N. Brantut,
n.brantut@ucl.ac.uk

Citation:
Brantut, N. (2021). Dilatancy toughening of shear cracks and implications for slow rupture propagation. *Journal of Geophysical Research: Solid Earth*, *126*, e2021JB022239. https://doi.org/10.1029/2021JB022239

Received 14 APR 2021
Accepted 30 OCT 2021

Abstract Dilatancy associated with fault slip produces a transient pore pressure drop which increases frictional strength. This effect is analyzed in a steadily propagating rupture model that includes frictional weakening, slip-dependent fault dilation and fluid flow. Dilatancy is shown to increase the stress intensity factor required to propagate the rupture tip. With increasing rupture speed, an undrained (strengthened) region develops near the tip and extends beyond the frictionally weakened zone. Away from the undrained region, pore fluid diffusion gradually recharges the fault and strength returns to the drained, weakened value. For sufficiently large rupture dimensions, the dilation-induced strength increase near the tip is equivalent to an increase in toughness that is proportional to the square root of the rupture speed. In general, dilation has the effect of increasing the stress required for rupture growth by decreasing the stress drop along the crack. Thermal pressurization has the potential to compensate for the dilatant strengthening effect, at the expense of an increased heating rate, which might lead to premature frictional melting. Using reasonable laboratory parameters, the dilatancy-toughening effect leads to rupture dynamics that is quantitatively consistent with the dynamics of observed slow slip events in subduction zones.

Plain Language Summary During fault slip, microscopic voids often open in the material forming the core of the fault, leading to a succion effect that can decompress the fluid present in the pores of the rock. This decompression strengthens the rock. At large scale, such a strengthening leads to an increase in the energy or load required to propagate the fault, leading to slower rupture speeds than otherwise anticipated.

1. Introduction

Dilatancy is a well documented process in intact, healed or overconsolidated rocks: due to shear deformation, microcavities (cracks, grain junctions) open, which induces an overall increase in porosity (Paterson & Wong, 2005, Section 5.3). In fluid saturated rocks, this increase in porosity has the potential to induce fluid pressure drops if the dilatant region is insufficiently drained, producing an increase in effective stress and thus strengthening the material. This phenomenon is called dilatancy hardening.

The importance of dilatancy hardening in fault mechanics has long been recognised in laboratory experiments and in theoretical rupture models. One of the first experimental evidence of dilatancy hardening in crustal rocks was obtained by Brace and Martin (1968) in diabase and granite, who showed that failure strength was increasing with increasing deformation rate as the deformation conditions became more undrained. Similar observations have been made on a range of low-porosity rocks (e.g., Chiu et al., 1983; Duda & Renner, 2013; Rutter, 1972). Martin (1980) further demonstrated that rock failure could be stabilized due to dilatancy, by considerably slowing down the deformation leading to strain localisation and fault slip. New laboratory results by Aben and Brantut (2021) have confirmed the direct stabilization of ruptures due to shear-induced dilation. Such work was focused on initially intact rock, where dilatancy is occurring in the bulk as well as within the incipient fault zone. In preexisting fault zones, dilatancy can be due to overriding asperities (along bare rock surfaces) and granular rearrangements (if gouge layers are present), leading to net fault zone opening during slip. Such behavior has been thoroughly documented in artificial fault gouges, for which dilatancy can be related to frictional state evolution (e.g., Marone et al., 1990; Samuelson et al., 2009; Sleep, 2006). Recent laboratory studies have shown that fault zone dilatancy (and compaction) exerts a first-order control on fluid pressure (Brantut, 2020; Faulkner et al., 2018; Lockner & Byerlee, 1994) and slip dynamics (Aben & Brantut, 2021; Proctor et al., 2020).

From a theoretical point of view, the role of dilatancy hardening in the propagation of shear rupture was initially investigated by Rice (1973), who showed that dilatancy tends to increase the fracture energy necessary to drive rupture propagation. Rice and Rudnicki (1979) demonstrated that dilatant hardening leads to a period of stable, quasi-static deformation prior to shear rupture instability. In a one dimensional (spring-slider) fault zone model in the context of slip-dependent strength and dilation, Rudnicki and Chen (1988) showed that dilatancy could prevent unstable fault motion. A similar stabilization effect was found by Segall and Rice (1995) for faults governed by rate and state dependent friction and dilation. For spatially extended fault slip, the competition between dilation, fluid flow and frictional weakening has been shown to produce slowly propagating slip events, in a manner and parameter range consistent with geophysical observations of slow slip in subduction zones (Liu, 2013; Liu & Rubin, 2010; Segall et al., 2010). Dilatancy has also been shown to promote quasi-static rupture propagation in coupled thermo-hydro-mechanical models where the weakening effect of thermal pressurization of pore fluid is limited by the strengthening effect of fault zone dilation (e.g., Suzuki & Yamashita, 2007, 2008, 2009).

Most of the aforementioned rupture models including the effect of fault zone dilation have relied on numerical solutions for either the quasi-static (Segall et al., 2010) or dynamic (Suzuki & Yamashita, 2008) equation of motion, effectively solving the fully coupled, nonlinear fracture problem without relying on specific assumptions regarding rupture process zones and weakening behavior. Liu and Rubin (2010) developed an energy balance approach based on fracture mechanics to determine analytical estimates for slip rate during slow slip transients, which compared well with their numerical results. The success of this approach is further justified by recent work by Barras et al. (2020); Garagash (2021) which demonstrated, in the context of rate and state friction laws, that nonlinear solutions to rupture problems could be recast in the framework of linear elastic fracture mechanics, where rupture propagation is governed by a Griffith-type criterion $G = G_c$, where G is the energy-release rate and G_c is a fracture energy that depends on rupture speed and parameters of the nonlinear friction law. Such a connection between nonlinear problems and linear elastic fracture mechanics equivalents was already highlighted by Ampuero and Rubin (2008); Hawthorne and Rubin (2013) for rate and state friction law. Estimates of fracture energy were also given by Segall et al. (2010, §78, 79 and 80) for the coupled, quasi-static, rate and state friction and dilatancy-diffusion problem. While those estimates are very useful to analyze simulation results *a posteriori*, they are expressed as a function of slip rate, which is *a priori* unknown in fracture problems. In order to use fracture energy in a Griffith energy balance $G = G_c$, or, equivalently, in a balance between stress intensity factor K and toughness K_c, and arrive at elementary predictions for rupture tip dynamics (a time and space history of the crack tip position), fracture energy or toughness would need to be expressed as a function of rupture speed instead of fault slip rate (as done recently by Garagash, 2021).

In addition to its potential impact on stability and fracture energy, one other key aspect of dilatancy in the context of rapid fault slip is its potential to counteract thermal pressurization of pore fluids and to accelerate heat production. This effect was explored extensively by Garagash and Rudnicki (2003), and some solutions of the coupled thermo-hydro-mechanical problem were exposed by Segall and Bradley (2012). For dilatancy occurring much more rapidly than shear heating, it amounts to resetting the pore pressure inside the fault at the onset of slip (Rice, 2006, §50), which increases the potential maximum temperature achieved during slip. This phenomenon plays a major role in determining the onset of frictional melting in low porosity, consolidated rocks (Brantut & Mitchell, 2018); in granite, dilatancy can indeed be so large as to rapidly decrease pore pressure down to vapor pressure during faulting and slip (Brantut, 2020). Recent laboratory measurements of fault zone dilatancy and hydraulic properties during dynamic rupture events (Brantut, 2020) highlight the need for a comprehensive assessment of the effect of dilatancy on rupture dynamics.

The present study focuses attention on the effects of fault zone dilatancy on the weakening and thermal response of the fault during dynamic slip, and aims to find a simple description of those effects in terms of fracture energy, to be used in a Griffith-type energy balance. Based on recent laboratory results (Aben & Brantut, 2021; Brantut, 2020), a simple slip-dependent weakening and porosity change model is used (similar to the approach of Rudnicki and Chen (1988)). Although more advanced parameterisations of weakening and dilation based on rate-and-state descriptions of friction have been determined experimentally at slow slip rates and used in theoretical investigations (e.g., Marone et al., 1990; Segall & Rice, 1995; Sleep, 2006; Samuelson et al., 2009), a direct dependence of friction and dilation on slip is a limit case of rate-and-state

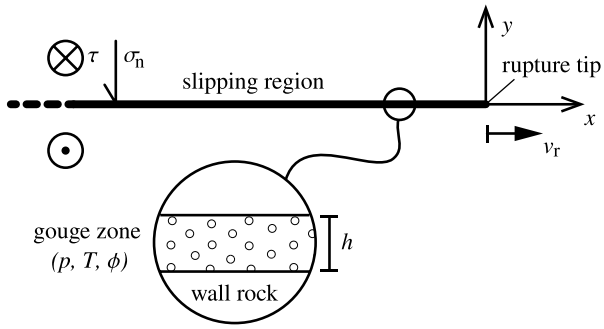

Figure 1. Schematic of the model setup, with dynamically propagating rupture at speed v_r along the x axis under anti-plane geometry. The internal structure of the fault is considered to be a porous material (gouge) of finite width (in the y direction), undergoing shear and dilation.

descriptions in response to sudden changes in slip rate, which is particularly relevant to rapid propagation of shear ruptures. A steadily propagating dynamic crack tip model is employed to arrive at semi-analytical results for shear stress, pore pressure and temperature evolution along the propagating rupture. Keeping with the eventual goal of finding a simple, usable form of fracture energy to use in a Griffith energy balance, a particular attention is paid to the contribution of fault zone dilation to fracture energy as a function of rupture propagation speed. This analysis leads to a refined description of the various contributions to fracture energy and energy release rate of different weakening processes, including "near-tip" mechanisms such as intrinsic frictional weakening or dilatancy, which contribute to G_c, and "far-tip" mechanisms like pore fluid diffusion or thermal pressurization (or decomposition, or melting), which are expected to contribute to G.

2. Model

2.1. Elastodynamics

Our main focus is to determine the relative contributions of slip-weakening, dilatancy and thermal pressurization in the energy balance of dynamic ruptures. A fully dynamic approach would require extensive numerical simulations, imposing somewhat arbitrary choices of initial and boundary conditions. For the purpose of making estimates of fracture energy and dissipation consistent with elastodynamics, it is useful to consider only the tip region of a dynamically propagating, steady-state, semi-infinite shear rupture (Viesca & Garagash, 2015). The steady-state assumption corresponds to an assumption of constant rupture speed v_r; it is valid when rupture speed varies only smoothly as a function of time, over distances (or timescales) much larger than the characteristic dimensions of the non-linear tip region. In a two dimensional configuration where the fault lies along the x axis (Figure 1), the shear stress τ at position $X = v_r t - x$ (in a reference frame moving with the rupture tip, see Figure 2b) is related to the slip rate distribution $V(X)$ as

$$\tau(X) = \tau_b + \frac{\bar{\mu}}{2\pi v_r} \int_0^\infty \frac{V(\xi)}{\xi - X} d\xi, \quad \text{(steady-state)} \tag{1}$$

where $\bar{\mu}$ is an apparent elastic modulus that depends on loading mode and rupture velocity. For semi-infinite ruptures, stress drop is neglected compared to strength variations and τ_b is set equal to the far-field residual shear strength on the fault. For simplicity, we only consider mode III (anti-plane) loading here; in this case $\bar{\mu} = F(v_r/c_s)\mu$ where μ is the shear modulus of the fault walls, c_s is the shear wave speed, and $F(z) = \sqrt{1 - z^2}$ (e.g., Rice, 1980). In the moving reference frame at constant speed v_r, the partial time

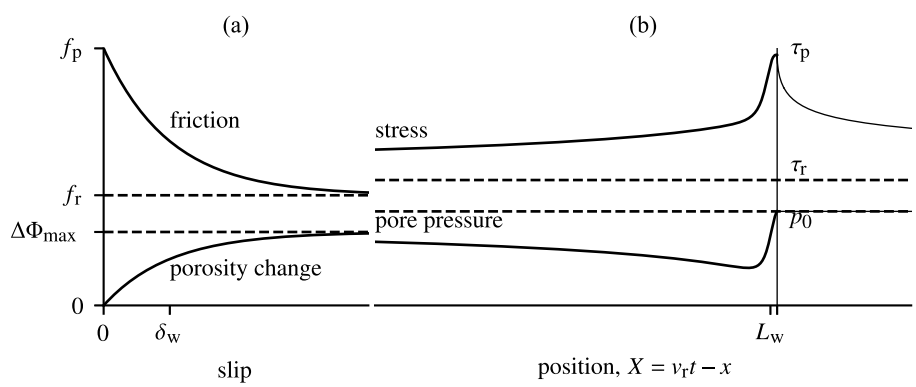

Figure 2. (a) Constitutive laws for friction and porosity evolution with slip (Equations 3 and 4); (b) Propagating crack model, with stress change due to both friction and pore pressure changes (Equation 2). The tip is mostly undrained, and recharge occurs at large distances.

derivatives are effectively derivatives with respect to coordinate X, $\partial/\partial t = (1/v_r)\partial/\partial X$, so that the dependent variables required to solve the dynamic problem are functions of X only.

2.2. Shear Strength

In the slipping part of the fault, the shear stress in Equation 1 must equal the shear strength of the fault. We assume that the fault is of finite width, filled with a porous material (Figure 1). It is initially saturated with a pore fluid, considered chemically inert at the timescale of the phenomena of interest here, at a uniform pressure $p = p_0$. The shear resistance to sliding, τ_f, is given by Terzaghi's effective stress principle,

$$\tau_f = f \times \sigma', \tag{2}$$

where $\sigma' = \sigma_n - p$ is the effective normal stress, σ_n is the applied normal stress, considered constant, and f is the friction coefficient.

The fault zone is assumed to be made of a consolidated material, for instance a healed cataclasite or fault gouge, so that shear strain produces significant (a) "direct" weakening of the fault by a decrease of the friction coefficient from a peak f_p to a residual value f_r, and (b) dilation of the fault, by way of microcrack opening and overriding of micro- and meso-scale asperities (e.g., Barton, 1976).

2.3. Slip Weakening Behavior

The former "direct weakening" effect has been thoroughly documented experimentally in consolidated or healed rocks (e.g., Karner et al., 1997; Nakatani & Scholz, 2004), and can be thought of as an irreversible decrease in cohesion; while the physical processes leading to the progressive degradation of strength with ongoing slip remain difficult to constrain in detail, it suffices for the present analysis to capture such a weakening effect as a simple progressive slip-weakening behavior for the friction coefficient (see a similar analysis in Rudnicki and Chen (1988); Figure 2a),

$$f(\delta) = f_r + (f_p - f_r)e^{-\delta/\delta_w}, \tag{3}$$

where δ denotes the total slip across the fault, and δ_w denotes a characteristic slip-weakening distance.

In the context of fast slip (with no subsequent healing), the frictional weakening as phenomenologically described by 3 is not fundamentally different from more elaborate formulations based on rate-and-state friction laws including rapid weakening at high slip rate, for instance due to flash heating (Brantut & Rice, 2011; Noda et al., 2009; Viesca & Garagash, 2015). For dynamic weakening, peak friction is typically of the order of 1 (or, 0.6 to 0.8 if we strictly follow Byerlee's rule of thumb), and weakened friction can be as low as 0.1, for instance due to asperity-scale thermal weakening (e.g., Rice, 2006; Di Toro et al., 2011). The slip weakening distance δ_w for dynamic weakening could be as small as a few 10s of μm (e.g., Brantut & Rice, 2011; Noda et al., 2009; Viesca & Garagash, 2015), but there is still considerable uncertainty in choosing this parameter in the phenomenological description 3.

At slower, sub-seismic slip rates, frictional weakening as in 3 is consistent with commonly used rate-and-state friction laws in rate-weakening materials and in the absence of healing: a sudden increase in slip rate does produce an exponential decay of the friction coefficient from a peak (proportional to the log of the velocity increase) to a residual value (proportional to the new "state" of the interface) (Scholz, 2002, chap. 2).

If we focus our attention to slip-weakening behavior observed in association with decreases in cohesion (e.g., during failure of intact or consolidated rocks), then appropriate values for peak frictional strength could be as high as 1.5, and the weakened friction coefficient is then of the order of 0.6–0.8 (Byerlee, 1978). The slip weakening distance δ_w typically associated with the failure process is of the order of 0.1–1 mm (e.g., Aben et al., 2019; Lockner et al., 2001; Ohnaka, 2003; Ohnaka & Shen, 1999; Wong, 1982).

2.4. Slip-Dependent Dilatancy

Fault zone dilation due to shear deformation is modeled following the approach of Rudnicki and Chen (1988), and we consider that the inelastic porosity change of the fault material depends directly on slip as (Figure 2a)

$$\Delta\Phi(\delta) = \Delta\Phi_{\max}(1 - e^{-\delta/\delta_D}), \tag{4}$$

where $\Delta\Phi_{max}$ is the maximum inelastic porosity change at large slip, and δ_D is a characteristic slip distance associated with the change in porosity.

A phenomenological relationship like 4 is supported by experimental data in consolidated rocks (e.g., Aben & Brantut, 2021; Barton, 1976; Brantut, 2020; Teufel, 1981). In this description, the parameter $\Delta\Phi_{max}$ can be thought of as the porosity change achieved when the fault zone material reaches critical state, that is, the stage at which further shear deformation does not impart any bulk volume change. In the case of dilatancy produced by shear rupture in consolidated rocks, the characteristic slip δ_D is likely commensurate to the slip weakening distance δ_w, since both the weakening and the dilatancy phenomena are driven by the same underlying processes (microcrack opening, linkage and slip). This was the case reported by Brantut (2020); Aben and Brantut (2021) in initially intact granite, where δ_D of the order of 1 mm was determined from volume change versus slip data.

The porosity evolution given by 4 is also compatible with the rate-and-state description given by Segall and Rice (1995) for faults subject to sudden changes in slip rate. In that framework, $\Delta\Phi_{max}$ is given by a dilatancy factor, of the order of 10^{-3}, multiplied to the log of the velocity step, and the characteristic slip δ_D is equal to the characteristic slip for state evolution, of the order of 10s of μm.

Overall, the phenomenological description 4 is consistent with both shear failure of consolidated materials and slip across preexisting discontinuities or gouge layers (in the "no-healing" limit), provided that the value of parameters $\Delta\Phi_{max}$ and δ_D are chosen accordingly. Such a versatile description, with a limited number of parameters, is useful to capture the essence of the dilatancy phenomenon.

2.5. Fluid Flow and Shear Heating

Due to dilatancy, frictional heating and hydraulic diffusion, the fault zone pore pressure p in 2 evolves as a function of time t during slip. The governing equations for thermal pressurization have been given numerous times in the literature, and only essential steps are recalled here. All notations directly follow those of Rice (2006); Garagash (2012). The conservation of fluid mass leads to the following governing equation for p (e.g., Rice, 2006):

$$\frac{\partial p}{\partial t} = \Lambda\frac{\partial\Theta}{\partial t} + \alpha_{hy}\frac{\partial^2 p}{\partial y^2} - \frac{1}{\beta^*}\frac{\partial n^{pl}}{\partial t}, \tag{5}$$

where Λ is the thermal pressurization coefficient, Θ is temperature, α_{hy} is the hydraulic diffusivity and β^* is a hydraulic storage capacity of the fault zone material. The local inelastic change in porosity is denoted n^{pl}. The coordinate y is oriented perpendicular to the fault plane (Figure 1), and we neglect along-fault fluid diffusion.

The temperature evolution of the fault zone is given by (Rice, 2006)

$$\frac{\partial\Theta}{\partial t} = \frac{\tau\dot{\gamma}}{\rho c} + \alpha_{th}\frac{\partial^2\Theta}{\partial y^2}, \tag{6}$$

where $\dot{\gamma}$ is the shear strain rate, ρc is the heat capacity and α_{th} is the thermal diffusivity.

The strain rate is assumed to follow a Gaussian profile of fixed width h across the fault (Garagash, 2012):

$$\dot{\gamma} = \frac{V}{h}\exp\left(-\frac{\pi y^2}{h^2}\right), \tag{7}$$

where V is the slip rate. The governing Equation 5 requires a local evolution of porosity at spatial position y, and we assume here that the local porosity rate $\partial n^{\mathrm{pl}}/\partial t$ is directly proportional to the strain rate, with a proportionality factor given by the derivative of 4 with respect to slip:

$$\frac{\partial n^{\mathrm{pl}}}{\partial t} = \Delta\Phi_{\max}(h/\delta_{\mathrm{D}})\dot{\gamma}e^{-\delta/\delta_{\mathrm{D}}}. \tag{8}$$

The formulation 8, together with 7, is consistent with expression 4 for the spatially averaged porosity across the fault. Note that the product $\Delta\Phi_{\max} \times h$ gives the maximum total fault zone opening due to inelastic dilation.

The solution for pore pressure at $y = 0$ as a function of time is given in integral form as (Garagash, 2012)

$$p(t) - p_0 = \frac{\Lambda}{\rho c h}\int_0^t \tau(t')V(t')\mathcal{K}\left(\frac{t-t'}{T^*};\frac{\alpha_{\mathrm{hy}}}{\alpha_{\mathrm{th}}}\right)dt' - \frac{1}{\beta^*}\int_0^t V(t')\Delta\Phi'[\delta(t')]\mathcal{A}\left(\frac{t-t'}{T_{\mathrm{hy}}}\right)dt', \tag{9}$$

where $\Delta\Phi'$ is the derivative 4 with respect to slip. The kernels $\mathcal{K}$ and $\mathcal{A}$ are given by Garagash (2012; Appendix A). The coupling between pore pressure and temperature introduces two diffusion timescales, a thermo-hydraulic one, $T^* = h^2/4\alpha$, where $\alpha = (\sqrt{\alpha_{\mathrm{hy}}} + \sqrt{\alpha_{\mathrm{th}}})^2$, and a purely hydraulic one, $T_{\mathrm{hy}} = h^2/4\alpha_{\mathrm{hy}}$. In addition, thermal pressurization introduces a natural weakening length scale which can be chosen as $\delta_{\mathrm{c}} = \rho c h/(f_{\mathrm{r}}\Lambda)$. Here, some flexibility exists in the definition of δ_{c} since friction coefficient is not constant; the choice of f_{r} is made to model the case when thermal pressurization becomes significant only at slip distances greater than δ_{w}, beyond which friction is in its weakened state (a similar assumption was used by Noda et al., 2009; Viesca & Garagash, 2015, in the case of early weakening by flash heating).

3. Dilatancy Toughening of Slip-Weakening Faults

Let us first consider the rupture problem without thermal pressurization, by assuming that Λ is very small, so that the slip weakening distance δ_{c} is much larger than both δ_{w} and δ_{D}. Such a situation would arise in fault zones with large pore space compressibility, which seems to be the case of fresh granitic faults as reported by Brantut (2020).

3.1. Effect of Dilatancy on Crack Tip Stress and Slip Rate

The coupled problem 2, 9 and 1 can be reformulated in terms of normalised quantities x/L_{w}, $\Delta\tau/\tau_{\mathrm{r}}$, V/V_{w} and $\delta/\delta_{\mathrm{w}}$, where $\Delta\tau = \tau - \tau_{\mathrm{r}}$ is the stress drop and

$$\tau_{\mathrm{r}} = f_{\mathrm{r}}\sigma_0', \quad L_{\mathrm{w}} = \frac{\bar{\mu}\delta_{\mathrm{w}}}{\tau_{\mathrm{r}}}, \quad V_{\mathrm{w}} = v_{\mathrm{r}}\delta_{\mathrm{w}}/L_{\mathrm{w}}. \tag{10}$$

The initial effective stress is denoted $\sigma_0' = \sigma_{\mathrm{n}} - p_0$. There are 4 parameters controlling the behavior of the system, the ratios

$$\frac{\delta_{\mathrm{D}}}{\delta_{\mathrm{w}}}, \quad f_{\mathrm{p}}/f_{\mathrm{r}}, \quad \frac{\Delta\Phi_{\max}}{\beta^*\sigma_0'}, \quad \text{and} \quad \frac{v_{\mathrm{r}}T_{\mathrm{hy}}}{L_{\mathrm{w}}} = \frac{h^2 v_{\mathrm{r}}\tau_{\mathrm{r}}}{4\alpha_{\mathrm{hy}}\bar{\mu}\delta_{\mathrm{w}}} = \frac{T_{\mathrm{hy}}}{T}, \tag{11}$$

where we denote $T = L_{\mathrm{w}}/v_{\mathrm{r}}$. The ratio $T_{\mathrm{hy}}/T = v_{\mathrm{r}}T_{\mathrm{hy}}/L_{\mathrm{w}}$ compares the hydraulic diffusion time to the characteristic time over which the slip-weakening region propagates along the fault, and is the key parameter controlling the transition from drained (small T_{hy}/T) to undrained (large T_{hy}/T) conditions near the rupture tip.

The solution is determined using the quadrature method detailed in Viesca and Garagash (2018). A set of solutions is presented in Figure 3, where constant $\delta_{\mathrm{D}}/\delta_{\mathrm{w}} = 1$ and $f_{\mathrm{p}}/f_{\mathrm{r}} = 2$ were chosen as representative values. For significant values of $\Delta\Phi/\beta^*\sigma_0'$ (i.e., a nonnegligible undrained de-pressurization due to dilatancy), we observe a clear transition from a drained regime at $T_{\mathrm{hy}}/T \ll 1$, where the crack tip behavior is essentially governed by the dry slip weakening mechanisms, to a dual scale behavior at $T_{\mathrm{hy}}/T \gg 1$ where the tip is undrained, governed by a slip-dependent behavior (combination of slip weakening and undrained effective stress law), and an extended region (at $x > v_{\mathrm{r}}T_{\mathrm{hy}}$) governed by the progressive pore pressure recharge of the fault zone from the off fault regions (see also Figure 2b). This second weakening behavior is purely diffusive,

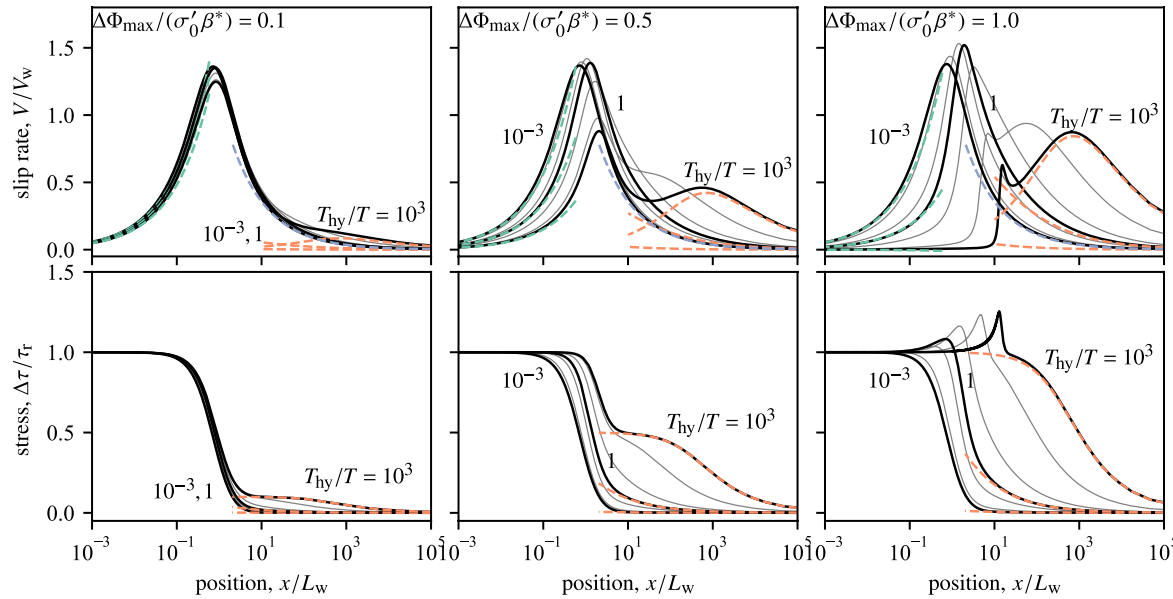

Figure 3. Slip rate (top) and strength (bottom) as a function of distance from the tip of a dynamically propagating crack for a range of undrained pore pressure change, parameter $\Delta\Phi_{max}/(\beta^*\sigma_0')$, and hydraulic diffusion time, parameter T_{hy}/T. Solutions are plotted for ×10 increments in parameter T_{hy}/T. Green dashed lines show the asymptotic behavior $V(x)/V_w = k \times (x/L_w)^{1/2}$, where k is constant that depends on the undrained strength and is obtained numerically for each solution; Blue dashed line is the LEFM asymptote $V(x)/V_w = 2/\sqrt{\pi} \times (x/L_w)^{-1/2}$ for the drained (dry) tip behavior; Orange dashed lines correspond to the purely diffusive asymptote given in Equations 12 and 13.

and at $x \gg v_r T_{hy}$ the strength is well approximated by (this follows from approximation of the second integral in 9, assuming concentrated source at $t = 0$):

$$\Delta\tau(x)/\tau_r \approx \frac{\Delta\Phi_{max}/(\beta^*\sigma_0')}{\sqrt{1 + \pi x/(v_r T_{hy})}}, \tag{12}$$

and the slip rate behaves as (this follows from inversion of the one-sided Hilbert transform in 1 and direct computation of the resulting integral)

$$V(x)/V_w \approx \frac{4}{\pi}\frac{\Delta\tau(x)}{\tau_r}\text{asinh}\left(\sqrt{\pi x/(v_r T_{hy})}\right). \tag{13}$$

With increasing undrained pore pressure change (parameter $\Delta\Phi_{max}/(\beta^*\sigma_0')$), the peak slip rate at the crack tip decreases, due to a smaller net strength drop under undrained conditions, while the slip rate in the extended "far-tip" region controlled by diffusive pore pressure recharge increases.

3.2. Stress Intensity Factor and Fracture Energy: Small Scale Yielding Approximation

Now equipped with a numerical solution and relevant asymptotes for the stress distribution along the moving crack, we can turn our attention to the desired analysis in terms of integrated fracture mechanics quantities. By construction, there is no stress or slip rate singularity at the tip of our moving crack. However, we can consider the situation where all the strength change due to the coupled slip weakening and dilation process occurs over a length scale much smaller than the finite size of the expanding crack. In that case, the stress distribution corresponds to a stress intensity factor that needs to be overcome for the crack to keep expanding, which is given by (Kostrov, 1966)

$$K_c = \sqrt{1 - v_r/c_s}\sqrt{\frac{2}{\pi}}\int_0^{c_s t}\frac{\Delta\tau(x, t - x/c_s)}{\sqrt{x}}dx. \tag{14}$$

In the quasi-static case ($v_r \ll c_s$), it simplifies to (Rice, 1980, pp. 598, 604)

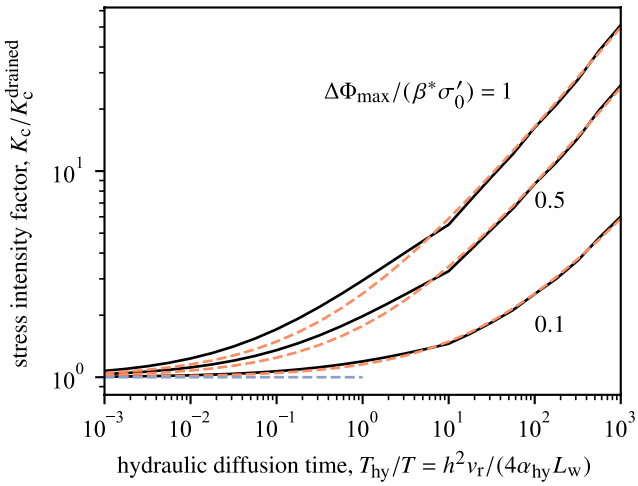

Figure 4. Stress intensity factor required to drive crack expansion, normalised by its perfectly drained value, as a function of hydraulic diffusion time relative to characteristic frictional weakening time. The cutoff length was set to $\ell_{cut} = \max\{100L_w, 10 \times v_r T_{hy}\}$ in the numerical computation. T_{hy}/T increases with increasing rupture speed. Blue dashed line indicates the purely drained limit. Orange dashed lines show the analytical estimate as computed from the sum of the drained end-member and the large T_{hy}/T end-member 18, using $\ell_{cut} = 10 \times v_r T_{hy}$.

$$K_c = \sqrt{\frac{2}{\pi}} \int_0^\infty \frac{\Delta\tau(x)}{\sqrt{x}} dx. \tag{15}$$

The purely drained end-member case, where $\Delta\tau$ is an exponentially decreasing function of slip, provides a lower bound $K_c^{drained}$ for the stress intensity factor. This lower bound is obtained from the finite fracture energy associated with the exponential slip-weakening process ($G_c^{drained} = \delta_w \sigma_0' (f_p - f_r)$):

$$K_c^{drained} = \sqrt{2\bar{\mu} G_c^{drained}} = \tau_r \sqrt{2L_w(f_p/f_r - 1)}, \tag{16}$$

where the relationship between stress intensity factor K and energy release rate G

$$K^2/2\bar{\mu} = G \tag{17}$$

was used. When dilatancy produces a significant pore pressure drop, the stress in the vicinity of the rupture tip increases, and thus K_c increases. The diffusive nature of the stress evolution introduces some surprising complexity in the problem: the integral of 15 does not converge. Following Rice (1973), a cutoff length ℓ_{cut} is introduced beyond which the strength is considered to be exactly zero, in accordance with the original assumption that all the strength evolution remains confined to a small region near the crack tip. The stress intensity factor computed this way exhibits a marked increase with increasing diffusion time relative to frictional weakening time T_{hy}/T, that is, with increasing rupture speed (Figure 4). Therefore, dilatancy produces an effective toughening of the fault, which potentially limits the rupture speeds. Using the approximation 12 for the stress distribution near the crack tip, the stress intensity factor is approximated by

$$K_c \approx 2\sqrt{\frac{2}{\pi}} \tau_r \frac{\Delta\Phi_{max}}{\beta^*\sigma_0'} \sqrt{v_r T_{hy}/\pi} \operatorname{asinh}\left(\sqrt{\pi \ell_{cut}/(v_r T_{hy})}\right) \qquad \text{(large } T_{hy}/T\text{)}. \tag{18}$$

This expression for stress intensity factor has a similar behavior to that derived by Rice (1973) for the case of an infinitesimally thin slipping zone and quasi-static rupture growth, where K was found to increase as $\sqrt{v_r}$, and a weak dependence on ℓ_{cut} was established.

A complementary approach to computing a critical stress intensity factor is to estimate the equivalent fracture energy associated with the weakening processes at the crack tip. Following Rice (2006), we can use a generalised form of fracture energy, better called "breakdown work," defined as

$$G'(\delta) = \int_0^\delta \tau(\delta') - \tau(\delta) d\delta', \tag{19}$$

which reduces to the conventional form established by Palmer and Rice (1973) when a well defined constant residual stress exists and slip is large compared to any characteristic slip-weakening distance. Under drained conditions, for instance at very small rupture speed ($T_{hy}/T \ll 1$), G' becomes almost constant at slip distances that are large compared to δ_w (Figure 5). In that case, $G' \approx G_c^{drained}$ and there is a well defined cohesive zone of small dimensions. With decreasing drainage (increasing T_{hy}/T), G' evolves in two distinct regimes: (a) an increase and stabilization up to slip distances of the order of δ_w, and (b) a marked increase

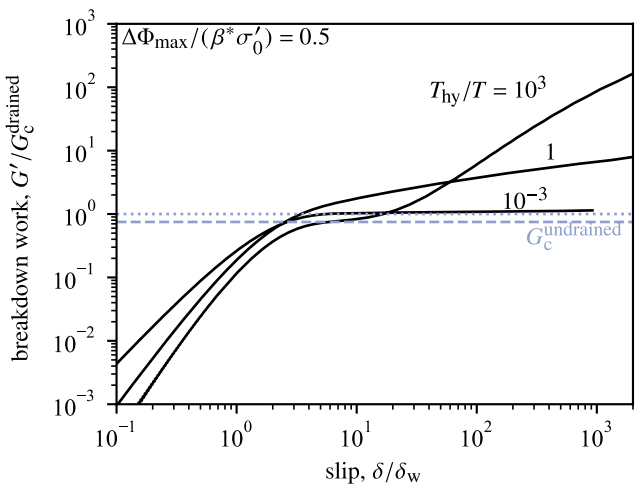

Figure 5. Breakdown work, normalised by its finite drained value, as a function of slip, for dynamic semi-infinite crack models computed using $f_p/f_r = 2$, $\Delta\Phi_{max}/(\beta^*\sigma_0') = 0.5$ and $\delta_D = \delta_w$.

with increasing slip beyond δ_w. The first regime corresponds to a purely undrained behavior, where shear strength evolves as

$$\tau_f = (f_r + (f_p - f_r)e^{-\delta/\delta_w})(\sigma_0' + (\Delta\Phi_{max}/\beta^*)(1 - e^{-\delta/\delta_D})) \qquad \text{(undrained)}. \tag{20}$$

The undrained behavior at the tip is associated to a well defined, constant fracture energy

$$G_c^{undrained} = (f_p/f_r - 1)\tau_r\delta_w \left(1 + \frac{\Delta\Phi_{max}/(\beta^*\sigma_0')}{\delta_D/\delta_w + 1}\right) - f_r\delta_D\Delta\Phi_{max}/\beta^*, \tag{21}$$

and the subsequent increase occurs due to diffusive recharge of the fault zone. The breakdown work, as computed by 19, does not converge to a fixed value at large slip: this is consistent with the theoretically infinite toughness and the requirement of a cutoff length ℓ_{cut} that limits the size of the cohesive zone. The unlimited increase in G' exhibited by our slip-weakening, dilatant fault zone model, is a general feature of weakening models limited by hydro-thermal diffusion processes (Rice, 2006; Brantut & Viesca, 2017; Viesca & Garagash, 2015).

For rupture propagating in consolidated rocks, using representative parameter values of $\delta_w \approx \delta_D \approx 1$ mm, $\mu \approx 30$ GPa, $(f_p/f_r - 1)\tau_r \approx 30$ MPa and $\alpha \approx 10^{-5}$ m^{2}s^{-1}, the key controlling parameter T_{hy}/T ranges from around 10^{-4} at $v_r \sim 1$ km/day up to 10 at $v_r \sim 2$ km/s when considering a relatively thin dilatant zone of $h = 1$ mm, and from 1 to 10^5 over the same rupture speed range when considering a thicker zone of $h = 10$ cm. For v_r approaching c_s, $\bar{\mu}$ vanishes and thus T_{hy}/T becomes unbounded. Therefore, for thin shear zones, dilatancy is expected to produce dramatic toughening only at dynamic rupture speeds, whereas large toughening is predicted even at small rupture speeds, of the order of 10 km/day, if dilatancy occurs in thick zones.

3.3. Stress Intensity Factor and Fracture Energy: "Near" and "Far"-Tip Contributions

While the toughening effect is somewhat intuitive, one caveat is that the concept of toughness and the relevance of the stress intensity factor to characterize crack expansion may be limited, since it relies on the small scale yielding assumption: in computing K_c and using it in terms of "crack resistance," one has to assume that the nonlinear end region, where the stress evolves from the nominal strength to the residual value, is small compared to the overall crack size. The need for a cutoff length ℓ_{cut} to prevent the mathematical divergence of the integral in 15 indicates that the nonlinear end region may not be small in general: it is only approximately true when the rupture dimensions are much larger than the drainage length scale ($v_r T_{hy}$).

In practice, for finite ruptures, the integral would extend along the full length of the rupture, making the toughness size-dependent (with longer ruptures having larger toughness than short ones). Size-dependent toughness is consistent with the results depicted in Figure 5 showing slip-dependent breakdown work: longer ruptures, which typically correspond to larger slip, have larger breakdown work. Such a size-dependence of toughness is commonly observed in engineering materials due to so-called crack bridging effects (e.g., Cox & Marshall, 1994). Here the matter is further complicated by the time-dependence of the strength evolution, which would make the toughness time-dependent as well.

An alternative to grouping all nonlinearities in the toughness and making it size- and time-dependent, is to separate the various contributions to stress intensity factor occurring at different scales. If some of the strength drop is not confined to a small region near the crack tip, which is the case when the rupture dimension is comparable to or smaller than the diffusion length scale, it will not contribute to toughness (or fracture energy) *per se*, but to the stress intensity factor (or energy release rate). Here, it is natural to have the nonlocal contribution of diffusive fault zone recharge into G, and keep the undrained contribution of dilatancy into G_c. In any case, the energy balance $G = G_c$ is always verified, but G now includes nonlinearities due to the constitutive behavior of the fault.

A simple illustrative example can be worked out: consider a semi-infinite crack along direction x, propagating at constant rupture speed v_r in a background stress field given by $\tau_b > 0$ for $x \geq 0$ and $\tau_b = 0$ for $X < 0$. The stress drop along the crack is $\tau_b - \tau_f$, and for sufficiently large diffusion time, the strength evolution τ_f can be split into a near tip, undrained contribution, and a spatially extended diffusive contribution. The near tip undrained contribution corresponds to an undrained toughness $K_c^{undrained} = \sqrt{2\bar{\mu}G_c^{undrained}}$. This toughness

must be matched by the stress intensity factor associated with the background loading, offset by the spatially extended diffusive contribution 12. This stress intensity factor, computed from 14, yields

$$K/\sqrt{1-v_r/c_s} = \sqrt{\frac{2}{\pi}}\left[2\sqrt{\ell}(\tau_b-\tau_r) - 2(f_r\Delta\Phi_{max}/\beta^*)\sqrt{v_rT_{hy}/\pi}\,\mathrm{asinh}(\pi\ell/(v_rT_{hy}))\right]. \quad (22)$$

In the limit $\ell \ll v_rT_{hy}$, the stress intensity factor is simply:

$$K/\sqrt{1-v_r/c_s} \approx \frac{2}{\sqrt{\pi}}\sqrt{2\ell}\left[\tau_b - f_r\Delta\Phi_{max}/\beta^* - \tau_r\right], \quad (\ell \ll v_rT_{hy}) \quad (23)$$

so that dilatancy has the effect of reducing the stress drop, and limiting the available energy for crack tip extension. By contrast, at large rupture dimensions ($\ell \gg v_rT_{hy}$), the stress intensity factor becomes

$$K/\sqrt{1-v_r/c_s} \approx \frac{2}{\sqrt{\pi}}\sqrt{2\ell}(\tau_b-\tau_r) - (f_r\Delta\Phi_{max}/\beta^*)\sqrt{2v_rT_{hy}}\ln\left(2\sqrt{\ell/(v_rT_{hy})}\right), \quad (\ell \gg v_rT_{hy}) \quad (24)$$

and the contribution of dilatancy eventually becomes negligible compared to that of the applied load.

The simple example of a semi-infinite crack propagating at constant speed is clearly not a fully realistic earthquake or slow-slip model, and the choice of applied load was made for mere mathematical convenience. However, it is quite illuminating to establish that dilatancy has a two-fold effect: (a) changing the fracture energy at the crack tip, and (b) reducing the stress drop and therefore the energy release rate in a time-dependent, diffusive manner. The different contributions of dilatancy and drainage can be recast in the Griffith energy balance,

$$G = K^2/2\bar{\mu} = G_c^{undrained}, \quad (25)$$

which provides an equation of motion for the crack tip through the dependency of G on v_r and crack tip position. The energy release rate G is thus impacted by the combination of applied load and diffusive pore pressure recharge along the crack, while the undrained behavior (combination of slip weakening and pore pressure drop) controls fracture energy. The energy release rate depends quadratically on K, and is therefore not simply offset by the diffusive pore pressure recharge far from the tip. Thus, in general, the full contribution of dilatancy and drainage to the dynamics of rupture is not simply a change in fracture energy. The approximation of small scale yielding made in the previous section (see Equation 18), which followed the developments of Rice (1973), is thus valid only in the limit of ruptures that extend well beyond the region impacted by pore pressure recharge.

3.4. Comparison to Dynamic Simulations

Whether due to a direct toughening effect, or to a reduction in energy release rate, dilatancy is expected to slow down rupture propagation. This can be tested in full elastodynamic simulations (see details in Appendix A). An illustrative example is shown in Figure 6, where key constitutive parameters were set to $\Delta\Phi_{max}/(\sigma_0'\beta^*) = 0.5$, $f_p/f_r = 2$, and the background stress outside the nucleation zone was set to $0.5\tau_r$ above the residual frictional strength. In that case, a purely undrained behavior would amount to zero stress drop, so that rupture should not grow unless drainage becomes significant (G, or K, is exactly zero under purely undrained conditions, cf. Equation 23). In the simulation, the rupture tip is indeed arrested at early times, at around $x/L_w' = 18$ (where $L_w' = \mu\delta_w/\tau_r$). The only mechanism that allows rupture to grow any further is the diffusive pore pressure recharge of the fault zone, which increases the strength drop in the interior of the crack, and increases the energy release rate. After its momentary arrest, rupture slowly accelerates, but remains well below the shear wave speed (the limiting speed in mode III) over the full simulation time, of the order of $400 \times \mu\delta_w/(\tau_r c_s)$. By comparison, simulated ruptures in the same background stress but without dilatancy accelerate to $v_r \approx c_s$ almost immediately after nucleation.

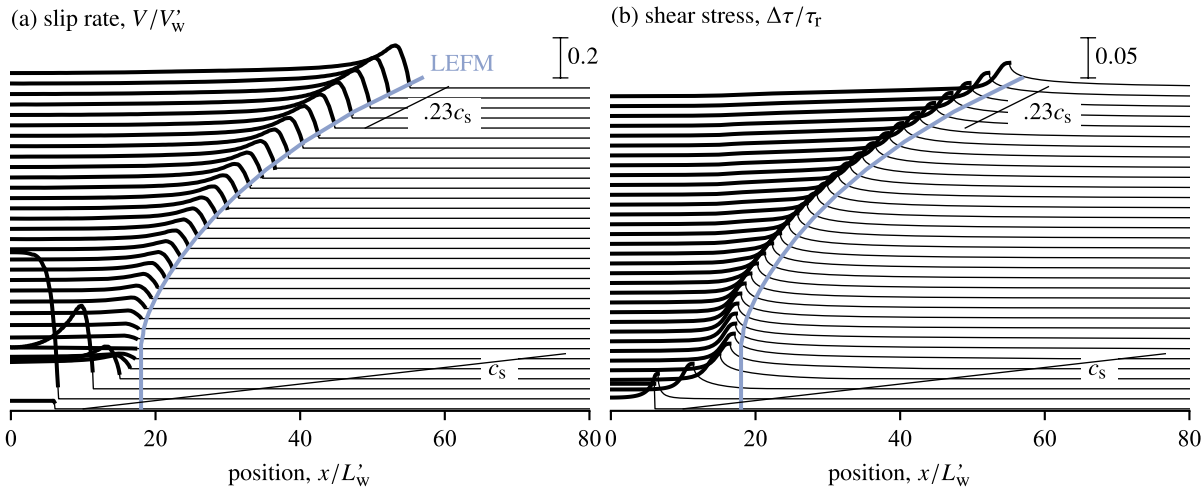

Figure 6. Slip rate (a) and stress (b) profiles during an elastodynamic rupture simulation with $\Delta\Phi_{max}/(\sigma_0'\beta^*) = 0.5$, $\delta_w = \delta_D$, $f_p = f_r$, and a normalised hydraulic diffusion time $T_{hy}/T' = 10^3$, where the characteristic frictional weakening time is defined as $T' = L_w'/c_s$, the characteristic distance is $L_w' = \delta_w \tau_r/\mu$, and the characteristic slip rate is $V_w' = \delta_w/T'$. The background stress was uniform at $1.5\tau_r$, except for a small region of size $12L_w'$ near the origin where its value was 1% above the peak strength. The rupture is symmetric with respect to $x = 0$ and only the domain $x > 0$ is displayed. Profiles are plotted at time intervals equal to $12.5T'$. Blue lines in each plot show the prediction of rupture tip trajectory from the Griffith energy balance.

The stress and slip rate near the tip of the spontaneous dynamic rupture are well characterized by the steady-state solution using the appropriate transient rupture speed (Figure 7). The tip is indeed under essentially undrained conditions, and the slip rate is reasonably well characterized by the linear elastic fracture mechanics (LEFM) solution $V/V_w = 2K_c^{undrained}/\sqrt{\pi} \times (x/L_w)^{-1/2}$, corresponding to the undrained stress intensity factor as defined by $K_c^{undrained} = \sqrt{2\bar{\mu}G_c^{undrained}}$. In the dynamic model, the progressive strength drop associated with drainage does not lead to a significant increase in slip rate further away from the tip (as predicted by the semi-infinite crack solution) due to the finite crack size of the model.

The usefulness of the LEFM approximation can be tested by comparing the rupture tip trajectory obtained from the full numerical solution to that based on the crack tip equation of motion arising from the Griffith energy balance. In view of the undrained behavior at the tip, it is appropriate to equate the dynamic energy release rate to the undrained fracture energy $G_c^{undrained}$, and to include the strength change due to pore fluid diffusion (given asymptotically by Equation 12 far from the tip) in the stress drop that enters in the expression of G (Equation 25). The details of the solution are given in Appendix B. The rupture tip trajectory resulting from this procedure is in remarkable agreement with the full numerical solution (Figure 6), illustrating the practical efficiency of the LEFM approximation.

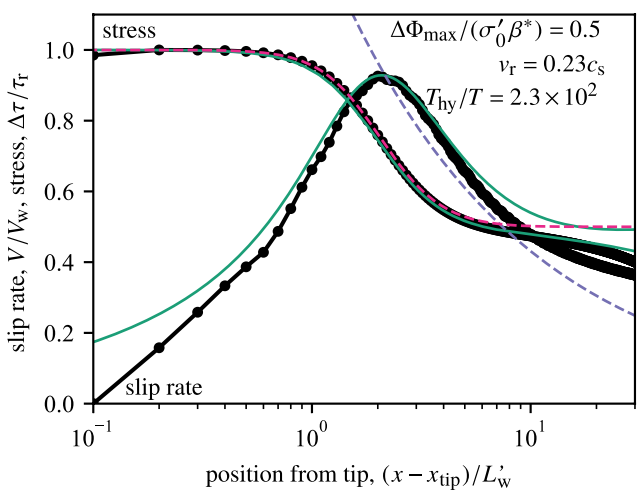

Figure 7. Slip rate and stress profile behind the crack tip during the last stage of the dynamic rupture shown in Figure 6, where rupture speed is approximately equal to $0.23c_s$ (black line and points), and steady-state semi-infinite crack solution (green) for the same parameter values. The blue dashed line is the LEFM prediction $V/V_w = 2K_c^{undrained}/\sqrt{\pi} \times (x/L_w)^{-1/2}$, and the red dashed line is the undrained strength prediction.

4. Link With Thermal Pressurization

In the previous Section we have established how dilatancy and pore fluid diffusion influence the dynamics of rupture, without regards to thermal effects. In general, thermal pressurization is expected to produce significant weakening for slip distances larger than δ_c. In granite gouge, δ_c is typically of the order of 10 mm (Brantut & Platt, 2017), which is around one order of magnitude larger than δ_w or δ_D. In freshly fractured granite, Brantut (2020) reported very high pore space compressibility compared to previously reported "mature" fault gouge material, which indicates that δ_c is likely much larger than the estimate of 10 mm in consolidated rocks.

In any case, thermal pressurization is not just superimposed onto the slip weakening and dilatancy processes, but is coupled with them: as noticed

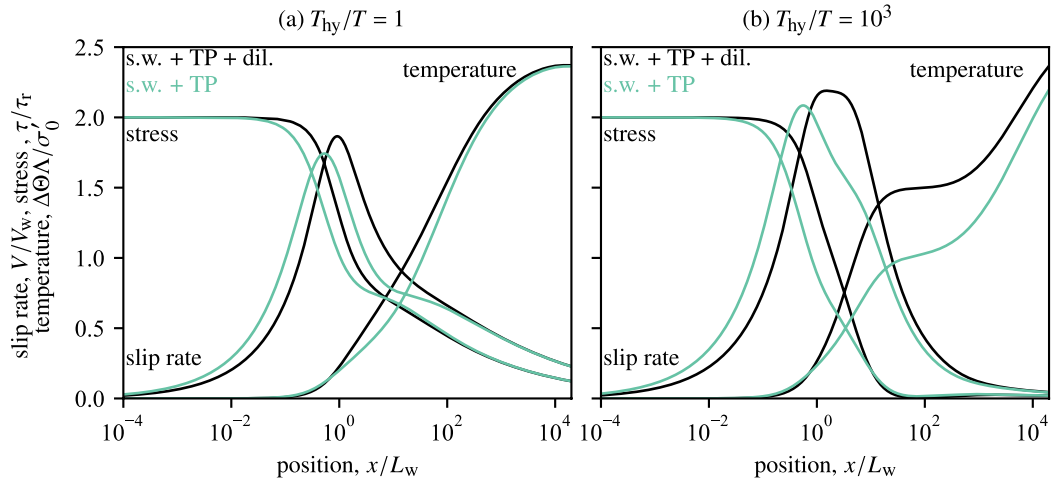

Figure 8. Slip rate, strength and temperature as a function of distance from the tip of a dynamically propagating crack driven by slip weakening friction, thermal pressurization, with (black lines, $\Delta\Phi_{max}/(\beta^*\sigma'_0) = 0.5$) and without (green lines, $\Delta\Phi_{max}/(\beta^*\sigma'_0) = 0$) dilatancy. Hydraulic diffusion time is set to $T_{hy}/T = 1$ (a) and $T_{hy}/T = 10^3$ (b).

by Garagash and Rudnicki (2003), the de-pressurization effect of dilatancy could be compensated by increased shear heating and fluid pressurization.

When dealing with the fully coupled slip weakening, dilatancy and thermal pressurization dynamic problem, a total of 6 nondimensional quantities control the system's behavior:

$$\frac{\delta_D}{\delta_w}, \quad f_p/f_r, \quad \frac{\Delta\Phi_{max}}{\beta^*\sigma'_0}, \quad \frac{T_{hy}}{T}, \quad \chi = \frac{\alpha_{hy}}{\alpha_{th}}, \text{ and } \quad \frac{\delta_c}{\delta_w} = \frac{\rho c h}{f_r \Lambda \delta_w}. \tag{26}$$

Let us consider a representative case by choosing $\delta_D/\delta_w = 1$, $f_p/f_r = 1$, $\chi = 10$, $\delta_c/\delta_w = 10$, and examine how dilatancy and hydro-thermal diffusion influence rupture dynamics, solving the steady-state problem (Equation 1 with 9, 3 and 4). When thermal pressurization is active, the residual strength is zero, so that the correct assumption to solve the semi-infinite rupture problem is that the applied stress is also zero.

In the absence of dilatancy and with relatively fast diffusion ($T_{hy}/T = 1$; Figure 8a), the stress evolution follows two stages of weakening, one associated with frictional weakening down to around $\tau/\tau_r = 1$ over a distance of the order of L_w, and a subsequent, slow decrease down to near 0 strength, associated with thermal pressurization. This is the situation presented in detail by Viesca and Garagash (2015, their figure 1b). When dilatancy is included, here choosing $\Delta\Phi_{max}/(\beta^*\sigma'_0) = 0.5$, a significant strengthening is observed and the first stage of weakening is effectively delayed. However, at large distance from the tip, strength, slip rate and temperature become indistinguishable from the nondilatant case. The weakening due to thermal pressurization is indeed similar between the two cases due to (a) the extra heating rate (temperature is initially higher in the dilatant case) in the undrained regime, and (b) the diffusive pore pressure recharge from the off-fault region.

The same general pattern is observed when diffusion time is larger ($T_{hy}/T = 10^3$, Figure 8b): an initial delayed weakening due to frictional slip weakening coupled to dilatancy, followed by weakening driven by thermal pressurization with an increased heating rate compared to the nondilatant case. The effect of dilatancy vanishes at distances $x \gg v_r T_{hy}$. When $\delta_D \ll \delta_c$ (as in the case shown in Figure 8), the adiabatic, undrained behavior including dilatancy is well described by a simple resetting of the initial pore pressure by the quantity $\Delta\Phi_{max}/\beta^*$ (Rice, 2006, §43); this is illustrated by the temperature rise, which is offset by $\Delta\Phi_{max}/(\beta^*\Lambda)$ compared to the nondilatant case (see Appendix C1), in the domain $L_w\delta_c/\delta_w < x < v_r T_{hy}$.

The main effect of dilatancy when coupled to thermal pressurization is a relative strengthening near the crack tip. This near-tip strengthening corresponds to an increase in breakdown work at small slip distances (Figure 9). Under purely undrained, adiabatic conditions (near the crack tip), there is a well defined fracture energy (the integral 19 converges). For constant friction coefficient, the fracture energy is simply

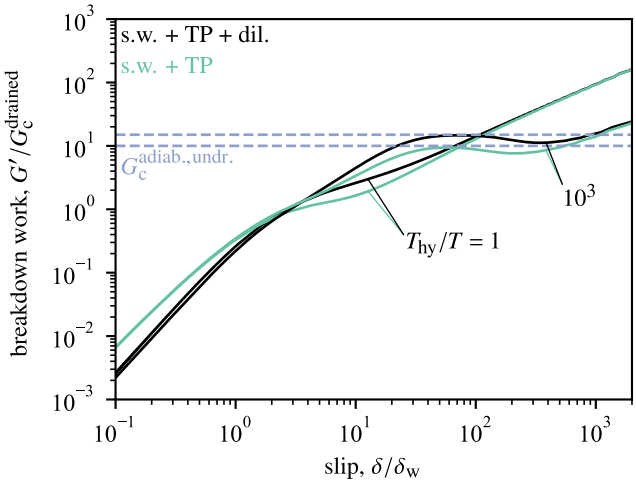

Figure 9. Breakdown work, normalised by its finite drained value, as a function of slip, for dynamic semi-infinite crack models computed using $f_p/f_r = 2$, $\delta_D/\delta_w = 1$, $\delta_c/\delta_w = 10$, $\chi = 10$, $T_{hy}/T = 1$ or 10^3, and with (black lines, $\Delta\Phi_{max}/(\beta^*\sigma_0') = 0.5$) or without (green lines, $\Delta\Phi_{max}/(\beta^*\sigma_0') = 0$) dilatancy. The dashed lines correspond to the fracture energy computed using 27 with and without dilatancy.

$$G_c^{adiab.,undr.} = \tau_r\delta_c(1 + \Delta\Phi_{max}/(\beta^*\sigma_0')), \quad \text{(constant friction)}, \qquad (27)$$

where it is easily seen how dilatancy is merely offsetting the effective stress. The fracture energy 27 is a good approximation for the breakdown work at small slip when diffusivity is low (Figure 9, dashed lines). For large rupture dimensions and large slip distances, hydro-thermal diffusion becomes significant and the effect of dilatancy on strength and breakdown work becomes progressively negligible (see curves merging in Figures 8 and 9).

Similarly to the situation where thermal pressurization was neglected, the continuous increase in breakdown work with increasing slip, at large distances from the crack tip, indicates that the weakening may not be confined to a well-defined small region near the crack tip. Thus, the breakdown work should not be given the meaning of "fracture energy" in the sense that it may not be used directly in a crack tip equation of motion of the kind $G = G_c$. Rather, as discussed in the previous section, if the weakening scales associated with friction, dilatancy and undrained, adiabatic thermal pressurization are much smaller than the length scale associated with hydro-thermal diffusion, one may separate the tip behavior and use the small scale yielding approximation to determine a constant fracture energy (e.g., $G_c^{adiab.,\ undr.}$), and the continued weakening far from the crack tip will then contribute to the stress intensity factor (or energy release rate).

Because dilatancy is expected to occur primarily over the first few millimeters of slip, concomitant with any frictional weakening process, its contribution is significant in the near-tip region. The key effect of dilatancy is therefore to increase the undrained fracture energy, which has the potential to locally slow down or stop rupture propagation.

5. Discussion

5.1. Onset of Vaporization and Melting

Throughout this paper the properties of the pore fluid have been assumed constant. This is a reasonable hypothesis when the fluid is a liquid, but the strong changes in pressure (and temperature) associated with dilatancy and thermal pressurization can significantly impact the fluid compressibility, thermal expansivity and heat capacity. Such changes have been invoked to explain slip dynamics in water saturated granite (Acosta et al., 2018), and recent experimental data have brought direct evidence for fluid vaporization (with dramatic increase in fluid compressibility) due to dilatancy during rock failure (Aben & Brantut, 2021; Brantut, 2020).

Is pore fluid vaporization a widespread phenomenon during rupture? A simple assessment was made by Brantut (2020) based on laboratory measurements of stick slip in granite, assuming isothermal and undrained conditions. Vaporization was predicted to occur at modest slip distances (less than 1 cm) under upper crustal conditions. This simple assessment can be revised by considering fluid diffusion and thermal pressurization, which tend to limit the pressure drop associated to dilatancy. The maximum pore pressure drop is given by $\Delta\Phi_{max}/\beta^*$, but a decreasing fraction of this maximum is achieved with increasing drainage and increasing contribution of thermal pressurization (Figure 10). In the case of freshly fracture granite reported by Brantut (2020), the slip weakening

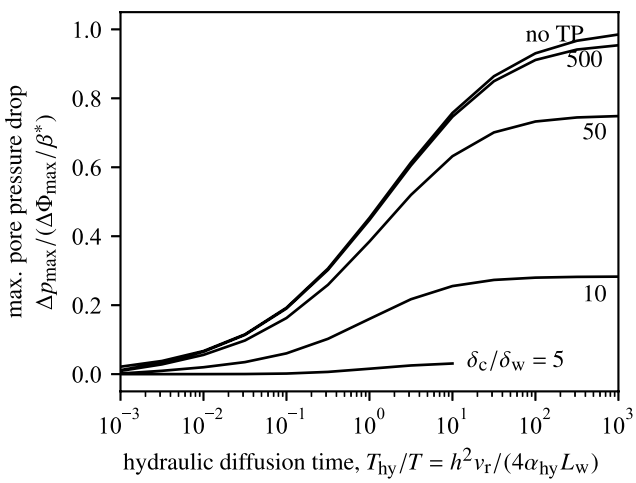

Figure 10. Maximum pore pressure drop Δp_{max} normalised by the undrained, isothermal pore pressure change $\Delta\Phi_{max}/\beta^*$ as a function of hydraulic diffusion time relative to characteristic rupture time. Parameter values are $f_p/f_r = 2$, $\delta_D/\delta_w = 1$, $\chi = 10$, $\Delta\Phi_{max}/(\beta^*\sigma_0') = 0.5$, and thermal pressurization slip weakening distance is changed as reported on the graph.

distance associated to thermal pressurization is most likely very large: the thermal pressurization factor Λ is small due to the large pore space compressibility of the newly formed gouge material, of the order of 10^{-8} Pa^{-1}. Combining this large compressibility with typical parameters for granite, using a fault thickness of 3 mm, a friction coefficient of 0.6, a heat capacity of 2.6 MPa/K and a thermal pressurization factor of $\Lambda = 0.03$ MPa/K, we find $\delta_c \approx 0.4$ m. This is indeed much larger than the inferred frictional slip weakening distance and characteristic slip associated with dilatancy, which are of the order of 1 mm. In that case, neglecting thermal pressurization to compute pore pressure drop is justified, and the maximum pore pressure drop should remain close to the undrained limit $\Delta\Phi_{max}/\beta^*$ if rupture is sufficiently fast (undrained tip). In laboratory experiments, direct measurements of pore pressure drop during faulting of intact granite are of the order of 30 MPa for slip of the order of 1 mm, so that vaporization is expected in roughly the upper 3 km of the crust in such rock type (Aben & Brantut, 2021; Brantut, 2020). With increasing temperature, the vaporization pressure increases up to the critical point, around 20 MPa at 370°C, so that vaporization could be expected down to 5 km depth. Such estimates are necessarily coarse, and strong local variations are expected due the natural roughness of faults (e.g., in large pull-apart regions).

When thermal pressurization is not efficient, as in the case of newly formed faults in granite, frictional heating is large, which can lead to melting of the fault material. The characteristic temperature rise for undrained, adiabatic behavior in the presence of rapid dilatancy at the onset of slip is given by $(\sigma_0' + \Delta\Phi_{max}/\beta^*)/\Lambda$ (see Appendix C1). At very large slip distances compared to δ_c, the effect of dilatancy becomes negligible (see Appendix C2). A thorough examination of the onset of melting during thermal pressurization was given by Rempel and Rice (2006); their analysis remains valid at large slip, and only needs to be amended at small slip by accounting for an initial offset in pore pressure equal to $\Delta\Phi_{max}/\beta^*$.

In the case of granite, the slip at which melting occurs is considerably shortened by dilatancy. For instance, at a depth of 5 km, assuming lithostatic normal stress and hydrostatic initial pore pressure, the initial effective stress is $\sigma_0' = 90$ MPa. With an average thermal pressurization factor of $\Lambda = 0.1$ MPa/K, intermediate between the low end-member value of 0.03 reported in Brantut (2020) for fresh fractures and a high end-member value of 0.3 MPa/K reported in Brantut and Platt (2017) for mature granite gouge, the adiabatic, undrained temperature rise is of 900 K. Melting is therefore expected only at slip distances several times larger than δ_c, (here a few centimeters if we assume a shear zone width of a few millimeters), well into the regime where strength is already significantly reduced by thermal pressurization. With a pressure drop due to dilatancy of the order of 30 MPa, commensurate to that measured in the laboratory, the adiabatic, undrained temperature rise becomes 1200 K, so that only a fraction of δ_c is required to trigger bulk melting of the shear zone, that is, before any significant strength reduction due to thermal pressurization.

Thus, dilatancy dramatically facilitates frictional melting. The common occurrence of pseudotachylytes in low-porosity, consolidated rocks (Sibson & Toy, 2006) is therefore expected not only because of the potential "dryness" of the initial material, but because dilatancy would either vaporise any preexisting fluid or trigger fast melting due to the induced pore pressure drop (see also Brantut & Mitchell, 2018, where this is discussed with an example from the field).

5.2. Diffusion-Driven Rupture Nucleation and Growth

As observed in dynamic simulations (see illustrative example in Figure 6), dilatancy has a dramatic impact on the dynamics of rupture during the nucleation phase. A thorough analysis of the transition from aseismic to seismic slip in slip-weakening, dilatant faults has been conducted by Ciardo and Lecampion (2019) in the context of injection-induced slip. Their analysis only considered along-fault fluid diffusion, assuming impermeable fault walls. Here, we considered the alternative hypothesis whereby only across-fault fluid flow was accounted for, which is reasonable when the pore pressure gradient along the x direction (which scales with $1/L_w$) is much smaller than that along the fault-perpendicular direction (which scales with $1/h$). Despite this difference, one important result of *Ciardo and Lecampion*'s analysis remains valid, and follows from the stress intensity factor computation given in Equation 22: there exists a minimum dilatancy amplitude above which rupture stabilization can occur, given by

$$\Delta\Phi_{max}^{c} = \beta^* \sigma_0' (\tau_b/\tau_r - 1). \tag{28}$$

At $\Delta\Phi_{max} > \Delta\Phi^{c}_{max}$, the undrained (isothermal) residual strength is above the background stress and rupture cannot propagate unless some fluid flows back into the fault zone. The rate of fault growth is then entirely determined by the rate of pore pressure recharge. The dynamic simulation shown in Figure 6 corresponds to the case $\Delta\Phi_{max} = \Delta\Phi^{c}_{max}$, and a exhibits a large nucleation timescale compared to typical elastodynamic timescales. In addition to the stabilizing effect due to offsets in residual strength in undrained conditions, dilatancy also has the potential to produce transient slip-strengthening behavior at the crack tip, which considerably increases the nucleation size of ruptures loaded with relatively uniform stress (Brantut & Viesca, 2015).

While a thorough analysis considering two-dimensional hydraulic diffusion and finite crack dimensions should eventually be conducted to make quantitative estimates of critical nucleation dimension and time, it is clear that dilatancy has a first order impact on fault stability and rupture initiation. Low porosity rocks, either intact, healed or sealed (e.g., granites) are the most affected by this process.

5.3. Dynamics of Slow Ruptures Driven by Dilatancy

In models based on rate and state friction laws, dilatancy hardening has been shown to be a viable mechanism for the generation and propagation of slow slip events in subduction zones (Segall et al., 2010). There are many characteristics of slow slip events that need to be explained quantitatively by any proposed physical model: spatio-temporal dynamics of events, recurrence rate, moment-duration relationship, relationship with earthquake location and timing, etc (e.g., Bürgman, 2018). Here, our very simple rupture model is not aimed at explaining all those observations; however, it is useful to test whether dilatancy hardening alone can explain the slowness of rupture propagation during slow slip events, and what parameter range would be required to do so.

Slow slip events in the Cascadia subduction zone typically propagate at speeds of the order of 10 km/day. Their spatial extent ranges from 50 to 100 km, and they are associated to stress drops ranging from 2 to 100 kPa (Michel et al., 2019; Schmidt & Gao, 2010). The stress intensity factor at the tip of such ruptures can be approximated by Hawthorne and Rubin (2013); Weng and Ampuero (2019)

$$K = \psi \Delta\tau \sqrt{W}, \tag{29}$$

where ψ is a geometrical constant (≈ 0.87 in the geometry used by Hawthorne and Rubin (2013), and given by $\approx\sqrt{2/\pi}$ for deeply buried antiplane faults according to (Weng & Ampuero, 2019)), $\Delta\tau$ is the stress drop and W is the width of the ruptured region. Using the spatial dimension and stress drop estimates from geodetic measurements, we obtain K ranging from 0.5 to 24 MPa m$^{1/2}$. This stress intensity factor has to be matched by the toughness that arises from frictional strength. Under purely drained conditions, the toughness is (Equation 16) $K_c^{\text{drained}} = \sqrt{2\mu\delta_w(f_p - f_r)\sigma_0'}$. For slow slip events in subduction zones, we can reasonably assume that the fault zone material is not overconsolidated or well cemented, so that conventional rate and state friction is an appropriate description of the strength. Our simplified model of purely slip-weakening friction corresponds to the "no-healing" end-member of the slip law (Garagash, 2021); in that approximation, the friction drop at the rupture tip is therefore of the order of $f_p - f_r \sim 10b$ (Garagash, 2021; Hawthorne & Rubin, 2013), where b is the evolution parameter of the friction law, itself of the order of 0.01. The slip weakening distance is of the order of 1–100 μm. The effective stress in the regions experiencing slow slip events is low, of the order of a few megapascals, as inferred by seismological observations (Bürgman, 2018, Section 2.3). Using a shear modulus of $\mu = 30$ GPa, we arrive at K_c^{drained} ranging from 0.1 to 1.7 MPa m$^{1/2}$, which overlaps with the K estimate only when very low stress drops are considered in conjunction with large slip weakening distances and effective stress. In addition, rupture events are not expected to be stable if we consider only a balance between K and K_c^{drained}, since any increase in K would lead to dynamic acceleration of the rupture tip (Weng, 2021). When dilatancy is accounted for, ruptures are stabilized since any increase in K and rupture speed can be matched by a corresponding increase in K_c (Figure 4; see below).

As rule of thumb, for any stabilization effect to be significant, that is, for K_c to increase significantly above K_c^{drained}, the magnitude of the undrained pore pressure drop has to be (at least) comparable to that of the stress drop. If dilatancy is the stabilizing process of slow slip events, we therefore expect the associated pore pressure drop to be, at the minimum, in the range 1–100 kPa.

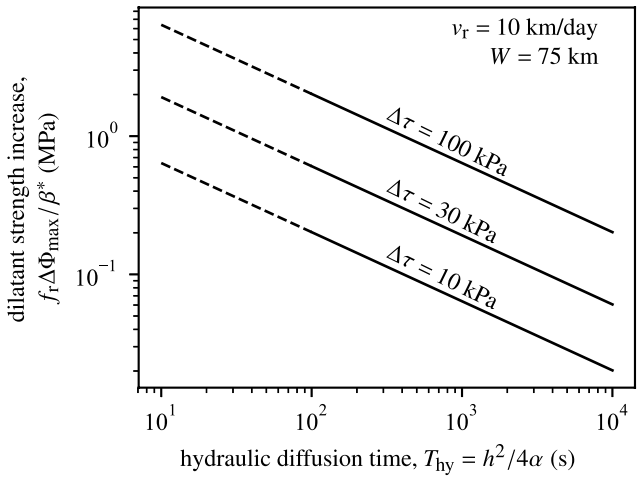

Figure 11. Combinations of dilatancy and diffusion parameters required to satisfy $K = K_c$ for slow slip events for a range of stress drops. The frictional contribution to toughness is neglected compared to that of dilatancy. Dashed lines correspond to hydraulic diffusion times such that the characteristic distance $v_r T_{hy}$ is smaller than typical frictional cohesive zone size, rendering the use of Equation 18 imprecise.

More precisely, the contribution of dilatancy and subsequent pore fluid diffusion can be estimated analytically using Equation 18, assuming that the hydraulic diffusion time T_{hy} is large compared to the elastodynamic timescale $T = \mu\delta_w/v_r(f_p - f_r)\sigma_0'$, that is, when the length scale $v_r T_{hy}$ is much larger than the frictional cohesive zone size. Choosing $\ell_{cut} = 10 \times v_r T_{hy}$ (or, alternatively, $\ell_{cut} = W$, with little quantitative impact on the result due to the weak dependency of K_c on the cuttoff length), we can look for the combination of parameters T_{hy} (hydraulic diffusion time) and $f_r\Delta\Phi_{max}/\beta^*$ (dilatant strength increase) required to match the stress intensity factor K estimated from geophysical data. For stress drops of the order of 30 kPa, rupture speeds of 10 km/day can be explained by a combination of $f_r\Delta\Phi_{max}/\beta^*$ = 0.3 to 0.1 MPa and $T_{hy} = h^2/4\alpha_{hy}$ = 300–3000 s, respectively (Figure 11). This corresponds to an undrained pore pressure drop at the rupture tip of the order of 0.1 MPa, so that only very modest dilatancy is required to severely limit the rupture speed, provided that diffusivity is low enough.

For a compressibility β^* of the order of 10^{-10} to 10^{-9} Pa^{-1}, a pressure drop of 0.1 MPa corresponds to a porosity change $\Delta\Phi_{max}$ from 10^{-3} to 10^{-2}%, which is commensurate with the dilatancy parameter ϵ inferred by Segall and Rice (1995) from Marone et al. (1990) data, and used by Segall et al. (2010) in their model for slow slip events. Even though the model used here is only slip-dependent and not directly rate-and-state dependent, both approaches point to relatively small dilatant effects (i.e., not of the order of tens of MPa as could be expected when fracturing intact material). Regarding pore fluid diffusion, in clay gouge, Faulkner et al. (2018) report diffusivities of the order of 10^{-8} m^2/s, so that shear zones of around 6 mm width would be sufficiently thick to obtain diffusion time consistent with the model. If diffusivity of the fault zone material is comparable to that reported for exhumed continental faults, $\alpha \approx 10^{-6}$ m^2/s (Wibberley & Shimamoto, 2003), considerably thicker shear zones of 6 cm would be needed to explain the rupture dynamics.

The parameter estimates obtained from our simple stress intensity factor analysis of slow slip events are realistic and consistent with laboratory measurements. As explained above, the rupture model used here is not designed to reproduce all the characteristics of slow slip events, but it does explain how slow rupture speeds can be achieved with dilatancy and pore fluid diffusion as the main control of strength.

Compared to the rate-and-state dependent approach used by Segall et al. (2010), the slip-dependent friction and porosity model we have employed is considerably simpler, but leads to similar rupture dynamics. The computation of K relies on the ruptures being confined in a strip of finite width (Hawthorne & Rubin, 2013), which is not part of the assumptions used by Segall et al. (2010). In a strictly two-dimensional configuration, the stress intensity factor is proportional to the squareroot of the rupture length. To see how ruptures might grow in this geometry, let us consider again, as in Section 3.3, a semi-infinite fault loaded by a background stress $\tau_b > 0$ in the region $x > 0$, and $\tau_b = 0$ elsewhere. At a given time t, the rupture has grown to a distance L in the loaded region, so that the stress intensity factor at the tip is

$$K = 2(\tau_b - \tau_r)\sqrt{\frac{2L}{\pi}}. \tag{30}$$

In the small scale yielding approximation with cutoff length $\ell_c = 10 \times v_r T_{hy}$, this stress intensity factor must equate the toughness given by Equation 18, which is proportional to $\sqrt{v_r} = \sqrt{dL/dt}$. Neglecting dynamic effects at small v_r, we arrive at the following differential equation for $L(t)$:

$$\frac{1}{L}\frac{dL}{dt} = \frac{1}{T_{hy}}\left[\frac{\tau_b - \tau_r}{f_r\Delta\Phi_{max}/\beta^*}\right]^2 \operatorname{asinh}^{-2}\left(\sqrt{\pi\ell_c/v_r T_{hy}}\right). \tag{31}$$

Assuming, as before, $\ell_c = 10 \times v_r T_{hy}$ (keeping in mind that the dependency on ℓ_{cut} is very weak), the last term in 31 is a constant, approximately equal to 0.17. The solution of 31 is thus an exponential growth:

$$L(t) = L(0)e^{t/t_g}, \tag{32}$$

where the growth rate is

$$t_g \sim 5.9 \times T_{hy}\left[\frac{f_r \Delta\Phi_{max}/\beta^*}{\tau_b - \tau_r}\right]^2. \tag{33}$$

Using the parameter values discussed above, with a stress drop of the order of $\tau_b - \tau_r = 0.01$ MPa, a dilatant strength contribution of the order of $f_r\Delta\Phi_{max}/\beta^* = 0.1$ MPa, and a diffusion time of $T_{hy} = 10^3$ s, we obtain a growth rate of $t_g \sim 5.9 \times 10^5$ s, that is, about one week. Such a timescale is commensurate to the total duration of slow slip events (e.g., Michel et al., 2019), and is much longer than any timescale associated with wave propagation along the fault. While the exponential growth might be viewed as unstable, the small growth rate, essentially governed by the diffusion timescale, makes these ruptures far less sensitive to variations in stress (or, energy release rate) compared to ruptures driven by constant toughness (or, fracture energy). In that sense, dilatancy produces relatively stable ruptures, which is consistent with observations of slow slip events in subduction zones.

6. Conclusions

By analyzing a crack model incorporating slip weakening friction and slip-dependent dilatancy coupled to fluid flow, we have established that dilatancy tends to limit crack propagation by increasing the stress intensity factor required for crack growth. At sufficiently large rupture speeds compared to the rate of fluid flow, the rupture tip is undrained, and the frictional strength is larger than in the nondilatant case. Further away from the tip fluid flow (i.e., pore pressure recharge) leads to a progressive decrease in strength back to the drained residual strength.

In a small-scale yielding approximation, the effect of dilatancy amounts to an increase in toughness that scales with the squareroot of rupture speed. This approximation is valid when the rupture dimension is much larger than the along-fault hydraulic diffusion length scale. For shorter rupture dimensions, the strength variations due to pore fluid diffusion are not confined in a small near-tip region, and the approximation of small-scale yielding becomes less accurate. Nevertheless, dilatancy still has the effect of increasing the applied stress intensity factor necessary for crack growth, which can be decomposed in a near-tip contribution (a relative decrease in toughness compared to the nondilatant regime) and a nonlocal contribution (a reduction in the net stress intensity factor) which includes a transition from undrained strength near the tip to the drained strength away from the tip. This natural decomposition of stress intensity factor into identifiable contributions does not have a simple parallel in terms of energy release rate and fracture energy, since G depends quadratically on K, which couples near-tip and "far"-tip effects.

When effective, thermal pressurization is seen to compensate somewhat the strengthening due to dilatancy through an increase in heating rate. The resulting temperature increase is transiently larger than in nondilatant cases, which can facilitate frictional melting. However, for large slip distances, the effect of dilation on temperature and strength vanishes due to thermo-hydraulic diffusion with the surrounding medium.

The dilatancy toughening effects analyzed here have direct applications in the study of the dynamics of slow slip events. A stress intensity factor analysis shows that the slowness of ruptures propagating in low effective stress regimes and with overall low stress drops, as in the case of slow slip events documented in the Cascadia subduction zone, can be explained using a simple fracture propagation model with a set of parameter values consistent with laboratory data. The relative stability of ruptures governed by slip weakening and dilatancy is linked to typically slow rupture growth rates, of the order of weeks, which is primarily controlled by the long hydraulic diffusion timescales inferred for slow slip events.

Appendix A: Elastodynamic Simulations

The elastodynamic equilibrium equation for 2D, mode III ruptures is

$$\tau(x,t) = \tau_b(x) - \frac{\mu}{2c_s}V(x,t) + \phi(x,t), \tag{A1}$$

where $\phi(x, t)$ corresponds to static and dynamic contributions to stress associated with a given slip rate history on the fault. The stress in A1 must be less than (if slip rate is zero) or equal to the fault strength (if slip rate is nonzero), given by Equation 2, together with governing Equations 3, 4, and 9.

Numerical solutions for stress and slip rate are determined by the method outlined in Brantut et al. (2019), and only the general principle is recalled here. Time and space are discretized with constant steps. At each time step, the previous slip rate history is used to compute the stress functional ϕ; the spatial convolution involved in this computation is performed in the Fourier domain. Then, the strength is evaluated by computing the pore pressure distribution along the fault, approximating the convolution integral in 9 by the mid-point rule. An estimate of slip rate at the next time step is then found by equating strength with stress. The procedure is then repeated, using the average between this estimate of slip rate and that from the previous time step in the computation of the stress transfer functional and pore pressure, to arrive at the final estimate of slip rate at the next time step. The evolution of friction coefficient and porosity in space and time is tracked by updating slip at each time and space step.

Space was discretized in 4,096 steps of size $\Delta x/L'_w = 1/10$, where we recall that $L'_w = \mu\delta_w/\tau_r$, and time was discretized in 8,192 steps of size $\Delta t = (1/2)\Delta x/c_s$. In the simulation illustrated in Figure 6, a uniform background stress equal to $\tau_b = 1.5\tau_r$ was used, and rupture was nucleated by setting $\tau_b = 1.01(f_p/f_r)\tau_r$ in a region of size $6L'_w$ around $x = 0$.

Appendix B: Rupture Tip Trajectory From LEFM

The energy balance is given by

$$G(v_r) = G_c^{\text{undrained}}, \tag{B1}$$

where the fracture energy is constant (Equation 21). The dynamic energy release rate is a function of rupture speed, and can be approximated by (e.g., Ampuero et al., 2006)

$$G(v_r) \approx \sqrt{\frac{1 - v_r/c_s}{1 + v_r/c_s}}\frac{K^2_{\text{static}}}{2\mu}, \tag{B2}$$

where K_{static} is the static stress intensity factor for the finite rupture in consideration, function of the current rupture tip positions and stress drop. Here we only consider symmetric ruptures, and denote the rupture tip position $a(t)$, so that the rupture speed is $v_r = da/dt$. The static stress intensity factor is

$$K_{\text{static}}(t,a) = \sqrt{\pi a}\frac{2}{\pi}\int_{-a}^{+a}\frac{\Delta\tau(x,t)}{\sqrt{a^2 - x^2}}dx, \tag{B3}$$

where the stress drop is

$$\Delta\tau(x,t) = \tau_b(x) - \tau_f(x,t). \tag{B4}$$

The frictional strength τ_f varies along the crack due to time-dependent diffusion of pore fluid after the passage of the rupture tip. All the near-tip slip-dependent, undrained contribution to strength has been accounted for in the undrained fracture energy and is thus not involved in the stress drop. At a given time t and position x ($|x| < |a|$), the strength is approximated by the large-time limit (Equation 12)

$$\tau_f(x,t) = \tau_r\frac{\Delta\Phi_{\max}/(\beta^*\sigma'_0)}{\sqrt{1 + (t - t_r(x))/T_{hy}}}, \tag{B5}$$

where $t_r(x)$ denotes the time at which the rupture tip was at position x, that is, t_r is the solution of $a(t) = x$.

The energy balance yields a delay differential equation for the rupture tip position,

$$\frac{da}{dt} = \frac{1 - \left(G_c^{\text{undrained}} / K_{\text{static}}(t, a)^2\right)^2}{1 + \left(G_c^{\text{undrained}} / K_{\text{static}}(t, a)^2\right)^2}, \tag{B6}$$

which is solved numerically using the Julia DifferentialEquations.jl package (Rackauckas & Nie, 2017). The integral in B3 is evaluated numerically using Gauss-Kronrod quadrature, and the time $t_r(x)$ is obtained by root finding (bisection method). The initial condition for a is set to $18 \times L'_w$, at the point of initial arrest immediately outside the nucleation zone.

Appendix C: Thermal Pressurization and Dilatancy

Here some closed-form solutions are presented for the thermal pressurization and dilatancy problem, with the assumption that the coefficient of friction remains constant. In that case, the solutions are sufficiently simple to allow clear physical interpretations.

Appendix C1: Adiabatic, Undrained Solution

Neglecting fluid and heat diffusion, the governing equations for pore pressure and temperature simplify into two ordinary differential equations for effective stress and temperature:

$$\frac{d\sigma'}{d\delta} = -\frac{\sigma'}{\delta_c} + \frac{\Delta\Phi_{\max}}{\beta^*}\frac{e^{-\delta/\delta_D}}{\delta_D}, \tag{C1}$$

$$\frac{d\Theta}{d\delta} = \frac{\sigma'}{\Lambda\delta_c}. \tag{C2}$$

Straightforward integration leads to the following solution:

$$\sigma'(\delta) = \sigma'_0 e^{-\delta/\delta_c} + \frac{\Delta\Phi_{\max}/\beta^*}{\delta_D/\delta_c}\left(e^{-\delta/\delta_D} - e^{-\delta/\delta_c}\right) \tag{C3}$$

for effective stress and

$$\Theta(\delta) = \Theta_0 + \frac{1}{\Lambda}\left[\sigma'_0(1 - e^{-\delta/\delta_c}) + \frac{\Delta\Phi_{\max}/\beta^*}{\delta_D/\delta_c}\left(\frac{\delta_D}{\delta_c}(e^{-\delta/\delta_D}) - (1 - e^{-\delta/\delta_c})\right)\right] \tag{C4}$$

for temperature. It is readily observed that the temperature asymptotically increases by a quantity $(\sigma'_0 + \Delta\Phi_{\max}/\beta^*)/\Lambda$ at large slip, so that dilatancy has the effect of resetting the initial effective stress, as reported by Rice (2006).

Appendix C2: Slip on a Plane, Constant Slip Rate Solution

For Gaussian shear strain rate profiles and dilatancy proportional to strain rate, the pore pressure evolution is given in integral form by

$$\begin{aligned} p(0,t) - p_0 = \frac{\Lambda}{\rho c}\int_0^t \tau(t')V\left[\frac{\alpha_{th}/(\alpha_{th} - \alpha_{hy})}{\sqrt{h^2 + 4\pi\alpha_{th}(t - t')}} - \frac{\alpha_{hy}/(\alpha_{th} - \alpha_{hy})}{\sqrt{h^2 + 4\pi\alpha_{hy}(t - t')}}\right]dt' \\ - \frac{1}{\beta^*}\int_0^t \frac{N(t')V}{\sqrt{h^2 + 4\pi\alpha_{hy}(t - t')}}dt', \end{aligned} \tag{C5}$$

where N is the rate of dilatant fault opening, given by $N/h = d\Delta\Phi/dt$. For vanishingly small h compared to both thermal and hydraulic boundary layer widths, the expression simplifies to

$$p(0,t) - p_0 = \frac{\Lambda}{2\rho c(\sqrt{\alpha_{\text{th}}} + \sqrt{\alpha_{\text{hy}}})} \int_0^t \frac{\tau(t')}{\sqrt{\pi(t-t')}} dt' - \frac{1}{2\beta^* \sqrt{\alpha_{\text{hy}}}} \int_0^t \frac{N(t')}{\sqrt{\pi(t-t')}} dt'. \tag{C6}$$

Further assuming constant friction and slip rate, we arrive at the following integral form for shear stress:

$$\tau(\delta) - \tau_0 = -\frac{1}{\sqrt{L^*}} \int_0^\delta \frac{\tau(\delta')}{\sqrt{\pi(\delta-\delta')}} d\delta' + \frac{1}{\sqrt{D}} \int_0^\delta \frac{N(\delta')/\beta^*}{\sqrt{\pi(\delta-\delta')}} d\delta', \tag{C7}$$

where $L^* = 4(\sqrt{\alpha_{\text{hy}}} + \sqrt{\alpha_{\text{th}}})^2 (\rho c / f_{\text{r}} \Lambda)^2 / V$ and $D = 4\alpha_{\text{hy}} / f_{\text{r}}^2 V$.

The specific form 4 for dilatancy can be rewritten in terms of fault zone opening as

$$N(\delta) = \Delta h / \delta_{\text{D}} e^{-\delta/\delta_{\text{D}}}, \tag{C8}$$

where Δh is the maximum opening, equivalent to $\Delta\Phi_{\text{max}} \times h$. The solution for shear stress can be found in the Laplace domain

$$\hat{\tau}(s) = \tau_0 \frac{\sqrt{L^*/s}}{1 + \sqrt{sL^*}} + \frac{\Delta h}{\delta_{\text{D}} \beta^*} \sqrt{\frac{L^*}{D}} \frac{1}{(1 + \sqrt{sL^*})(s + 1/\delta_{\text{D}})}, \tag{C9}$$

where $\hat{\tau}$ denotes the Laplace transform of shear stress and s is the transformed independent variable. By standard inversion technique we find the following solution in terms of slip:

$$\tau(\delta) = \tau_0 \exp\left(\frac{\delta}{L^*}\right) \text{erfc}\left(\sqrt{\frac{\delta}{L^*}}\right) + \frac{\Delta h}{\delta_{\text{D}} \beta^*} \sqrt{\frac{L^*}{D}} \frac{1}{1 + L^*/\delta_{\text{D}}} \left[-\exp\left(\frac{\delta}{L^*}\right) \text{erfc}\left(\sqrt{\frac{\delta}{L^*}}\right) + \right.$$
$$\left. \exp\left(-\frac{\delta}{\delta_{\text{D}}}\right) \left(1 + \sqrt{\frac{L^*}{\delta_{\text{D}}}} \text{erfi}\left(\sqrt{\frac{\delta}{\delta_{\text{D}}}}\right)\right)\right]. \tag{C10}$$

Reintroducing $\Delta\Phi_{\text{max}} = \Delta h / h$, and denoting

$$\tau_{\text{D}} = \frac{\Delta h}{\delta_{\text{D}} \beta^*} \sqrt{\frac{L^*}{D}} = \frac{f_{\text{r}} \Delta\Phi_{\text{max}}}{\beta^*} \frac{\delta_{\text{c}}}{\delta_{\text{D}}} \left(1 + \sqrt{\frac{\alpha_{\text{th}}}{\alpha_{\text{hy}}}}\right),$$

the shear stress can be rewritten with more easily recognizable quantities as

$$\tau(\delta) = \tau_0 \exp\left(\frac{\delta}{L^*}\right) \text{erfc}\left(\sqrt{\frac{\delta}{L^*}}\right) + \frac{\tau_{\text{D}}}{1 + L^*/\delta_{\text{D}}} \left[-\exp\left(\frac{\delta}{L^*}\right) \text{erfc}\left(\sqrt{\frac{\delta}{L^*}}\right) + \right.$$
$$\left. \exp\left(-\frac{\delta}{\delta_{\text{D}}}\right) \left(1 + \sqrt{\frac{L^*}{\delta_{\text{D}}}} \text{erfi}\left(\sqrt{\frac{\delta}{\delta_{\text{D}}}}\right)\right)\right]. \tag{C11}$$

In the slip on a plane, constant slip rate assumption, the temperature evolution is given by

$$\Theta(\delta) - \Theta_0 = \frac{1}{2\rho c} \sqrt{\frac{V}{\alpha_{\text{th}}}} \int_0^\delta \frac{\tau(\delta')}{\sqrt{\pi(\delta-\delta')}} d\delta'. \tag{C12}$$

Using again Laplace transforms and after a lengthy but straightforward calculation, we arrive at

$$\Theta(\delta) - \Theta_0 = \frac{1}{f_{\text{r}} \Lambda} \left(1 + \sqrt{\frac{\alpha_{\text{hy}}}{\alpha_{\text{th}}}}\right) \left[\tau_0 - \tau(\delta) + \tau_{\text{D}} \sqrt{\frac{\delta_{\text{D}}}{L^*}} e^{-\delta/\delta_{\text{D}}} \text{erfi}\left(\sqrt{\frac{\delta}{\delta_{\text{D}}}}\right)\right]. \tag{C13}$$

The main interest of closed form expressions C11 and C13 is that they show that (a) shear stress approaches zero and (b) temperature approaches $\sigma_0'(1 + \sqrt{\alpha_{\text{hy}}/\alpha_{\text{th}}})/\Lambda$ at large slip. The latter asymptote is the same as that without dilatancy (Rice, 2006). The effect of dilatancy is thus *not* simply to reset the initial pore pres-

sure: since dilatancy only occurs within the fault, pore pressure will spontaneously reequilibrate with the surrounding medium, so that at large time the effect of dilatancy becomes insignificant.

Data Availability Statement

The results of this paper can be reproduced by direct implementation of the analytical formulae and numerical methods described in the main text and appendices; no new data were generated in this work.

Acknowledgments
Discussions with Frans Aben, Dmitry Garagash, Jessica Hawthorne, Jim Rice and Rob Viesca helped shaping this work. Useful suggestions and comments from Huihui Weng and an anonymous reviewer contributed to improve the manuscript. Support from the UK Natural Environment Research Council (grants NE/K009656/1 and NE/S000852/1) and from the European Research Council under the European Union's Horizon 2020 research and innovation programme (project RockDEaF, grant agreement #804685), is gratefully acknowledged.

References

Aben, F. M., & Brantut, N. (2021). Dilatancy stabilises shear failure in rock. *Earth and Planetary Science Letters*, *574*, 117–174. https://doi.org/10.1016/j.epsl.2021.117174

Aben, F. M., Brantut, N., Mitchell, T. M., & David, E. C. (2019). Rupture energetics in crustal rock from laboratory-scale seismic tomography. *Geophysical Research Letters*, *46*, 7337–7344. https://doi.org/10.1029/2019GL083040

Acosta, M., Passelègue, F. X., Schubnel, A., & Violay, M. (2018). Dynamic weakening during earthquakes controlled by fluid thermodynamics. *Nature Communications*, *9*, 3074. https://doi.org/10.1038/s41467-018-05603-9

Ampuero, J.-P., Ripperger, J., & Mai, P. M. (2006). Properties of dynamic earthquake ruptures with heterogeneous stress drop. In R. Abercrombie, A. McGarr, G. Di Toro, & H. Kanamori (Eds.), *Earthquakes: Radiated energy and the physics of faulting, Geophys. Monogr. Ser*. (Vol. *170*, pp. 255–261): American Geophysical Union. https://doi.org/10.1029/170gm25

Ampuero, J.-P., & Rubin, A. M. (2008). Earthquake nucleation on rate and state faults—Aging and slip laws. *Journal of Geophysical Research*, *113*, B01302. https://doi.org/10.1029/2007JB005082

Barras, F., Aldam, M., Roch, T., Brener, E. A., Bouchbinder, E., & Molinari, J.-F. (2020). The emergence of crack-like behavior of frictional rupture: Edge singularity and energy balance. *Earth and Planetary Science Letters*, *531*, 115978. https://doi.org/10.1016/j.epsl.2019.115978

Barton, N. (1976). The shear strength of rock and rock joints. *International Journal of Rock Mechanics and Mining Science & Geomechanics Abstracts*, *13*, 255–279. https://doi.org/10.1016/0148-9062(76)90003-6

Brace, W. F., & Martin, R. J. (1968). A test of the law of effective stress for crystalline rocks of low porosity. *International Journal of Rock Mechanics and Mining Sciences*, *5*, 415–426. https://doi.org/10.1016/0148-9062(68)90045-4

Brantut, N. (2020). Dilatancy-induced fluid pressure drop during dynamic rupture: Direct experimental evidence and consequences for earthquake dynamics. *Earth and Planetary Science Letters*, *538*, 116179. https://doi.org/10.1016/j.epsl.2020.116179

Brantut, N., Garagash, D. I., & Noda, H. (2019). Stability of pulse-like earthquake ruptres. *Journal of Geophysical Research*, *124*, 8998–9020. https://doi.org/10.1029/2019JB017926

Brantut, N., & Mitchell, T. M. (2018). Assessing the efficiency of thermal pressurisation using natural pseudotachylyte-bearing rocks. *Geophysical Research Letters*, *45*, 9533–9541. https://doi.org/10.1029/2018GL078649

Brantut, N., & Platt, J. D. (2017). Dynamic weakening and the depth dependence of earthquake faulting. In M. Y. Thomas, T. M. Mitchell, & H. S. Bhat (Eds.), *Fault zone dynamic processes: Evolution of fault properties during seismic rupture, Geophys. Monogr. Ser*. (Vol. *227*, pp. 171–194): American Geophysical Union. https://doi.org/10.1002/9781119156895.ch9

Brantut, N., & Rice, J. R. (2011). How pore fluid pressurization influences crack tip processes during dynamic rupture. *Geophysical Research Letters*, *38*, L24314. https://doi.org/10.1029/2011GL050044

Brantut, N., & Viesca, R. C. (2015). Earthquake nucleation in intact or healed rocks. *Journal of Geophysical Research*, *119*, 191–209. https://doi.org/10.1002/2014JB011518

Brantut, N., & Viesca, R. C. (2017). The fracture energy of ruptures driven by flash heating. *Geophysical Research Letters*, *44*, 6718–6725. https://doi.org/10.1002/2017GL074110

Bürgman, R. (2018). The geophysics, geology and mechanics of slow fault slip. *Earth and Planetary Science Letters*, *495*, 112–134. https://doi.org/10.1016/j.epsl.2018.04.062

Byerlee, J. D. (1978). Friction of rocks. *Pure and Applied Geophysics*, *116*, 615–626. https://doi.org/10.1007/bf00876528

Chiu, H. K., Johnston, I. W., & Donald, I. B. (1983). Appropriate techniques for triaxial testing of saturated soft rock. *International Journal of Rock Mechanics and Mining Science & Geomechanics Abstracts*, *20*(3), 107–120. https://doi.org/10.1016/0148-9062(83)91301-3

Ciardo, F., & Lecampion, B. (2019). Effect of dilatancy on the transition from aseismic to seismic slip due tot fluid injection in a fault. *Journal of Geophysical Research*, *124*, 3724–3743. https://doi.org/10.1029/2018jb016636

Cox, B. N., & Marshall, D. B. (1994). Concepts for bridged cracks in fracture and fatigue. *Acta Metallurgica et Materialia*, *42*(2), 341–363. https://doi.org/10.1016/0956-7151(94)90492-8

Di Toro, G., Han, R., Hirose, T., De Paola, N., Nielsen, S., Mizoguchi, K., et al. (2011). Fault lubrication during earthquakes. *Nature*, *471*, 494–498. https://doi.org/10.1038/nature09838

Duda, M., & Renner, J. (2013). The weakening effect of water on the brittle failure strength of sandstone. *Geophysical Journal International*, *192*, 1091–1108. https://doi.org/10.1093/gji/ggs090

Faulkner, D. R., Sanchez-Roa, C., Boulton, C., & den Hartog, S. A. M. (2018). Pore fluid pressure development in compacting fault gouge in theory, experiments, nature. *Journal of Geophysical Research*, *123*, 226–241. https://doi.org/10.1002/2017jb015130

Garagash, D. I. (2012). Seismic and aseismic slip pulses driven by thermal pressurization of pore fluid. *Journal of Geophysical Research*, *117*. B04314. https://doi.org/10.1029/2011JB008889

Garagash, D. I. (2021). Fracture mechanics of rate-and-state faults and fluid injection induced slip. *Philosophical Transactions of the Royal Society A: Mathematical*, *379*, 20200129. https://doi.org/10.1098/rsta.2020.0129

Garagash, D. I., & Rudnicki, J. W. (2003). Shear heating of a fluid-saturated slip-weakening dilatant fault zone 1. Limiting regimes. *Journal of Geophysical Research*, *108*(B2), 2121. https://doi.org/10.1029/2001JB001653

Hawthorne, J. C., & Rubin, A. M. (2013). Laterally propagating slow slip events in a rate and state friction model with a velocity-weakening to velocity-strengthening transition. *Journal of Geophysical Research*, *118*, 3785–3808. https://doi.org/10.1002/jgrb.50261

Karner, S. L., Marone, C., & Evans, B. (1997). Laboratory study of fault healing and lithification in simulated fault gouge under hydrothermal conditions. *Tectonophysics*, *277*, 41–55. https://doi.org/10.1016/s0040-1951(97)00077-2

Kostrov, B. V. (1966). Unsteady propagation of longitudinal shear cracks. *Journal of Applied Mathematics and Mechanics*, *30*, 1241–1248. https://doi.org/10.1016/0021-8928(66)90087-6
Liu, Y. (2013). Numerical simulations on megathrust rupture stabilized under strongdilatancy strengthening in slow slip region. *Geophysical Research Letters*, *40*, 1311–1316. https://doi.org/10.1002/grl.50298
Liu, Y., & Rubin, A. M. (2010). Role of fault gouge dilatancy on aseismic deformation transients. *Journal of Geophysical Research*, *115*, B10414. https://doi.org/10.1029/2010JB007522
Lockner, D. A., & Byerlee, J. D. (1994). Dilatancy in hydraulically isolated faults and the suppression of instability. *Geophysical Research Letters*, *21*(22), 2353–2356. https://doi.org/10.1029/94gl02366
Lockner, D. A., Byerlee, J. D., Kuksenko, V., Ponomarev, A., & Sidorin, A. (2001). Quasi-static fault growth and shear fracture energy in granite. *Nature*, *350*(6313), 39–42.
Marone, C., Raleigh, C. B., & Scholz, C. H. (1990). Frictional behavior and constitutive modeling of simulated fault gouge. *Journal of Geophysical Research*, *95*(B5), 7007–7025. https://doi.org/10.1029/jb095ib05p07007
Martin, R. J. (1980). Pore pressure stabilization of failure in Westerly granite. *Geophysical Research Letters*, *7*(5), 404–406. https://doi.org/10.1029/gl007i005p00404
Michel, S., Gualandi, A., & Avouac, J.-P. (2019). Similar scaling laws for earthquakes and Cascadia slow-slip events. *Nature*, *574*, 522–526. https://doi.org/10.1038/s41586-019-1673-6
Nakatani, M., & Scholz, C. H. (2004). Frictional healing of quartz gouge under hydrothermal conditions: 1. Experimental evidence for solution transfer healing mechanism. *Journal of Geophysical Research*, *109*, B07201. https://doi.org/10.1029/2001JB001522
Noda, H., Dunham, E. M., & Rice, J. R. (2009). Earthquake ruptures with thermal weakening and the operation of major faults at low overall stress levels. *Journal of Geophysical Research*, *114*, B07302. https://doi.org/10.1029/2008JB006143
Ohnaka, M. (2003). A constitutive scaling law and a unified comprehension for frictional slip failure, shear fracture of intact rock, and earthquake rupture. *Journal of Geophysical Research*, *108*(B2), 2080. https://doi.org/10.1029/2000JB000123
Ohnaka, M., & Shen, L. (1999). Scaling of the shear rupture process from nucleation to dynamic propagation: Implications of geometry irregularity of the rupturing surfaces. *Journal of Geophysical Research*, *104*(B1), 817–844. https://doi.org/10.1029/1998jb900007
Palmer, A. C., & Rice, J. R. (1973). The growth of slip surfaces in the progressive failure of over-consolidated clay. *Proceedings of the Royal Society of London A.*, *332*, 527–548.
Paterson, M. S., & Wong, T. F. (2005). *Experimental rock deformation—The brittle field* (2nd ed.). Springer-Verlag.
Proctor, B., Lockner, D. A., Kilgore, B. D., Mitchell, T. M., & Beeler, N. M. (2020). Direct evidence for fluid pressure, dilatancy, and compaction affecting slip in isolated faults. *Geophysical Research Letters*, *47*, 767, e2019GL086. https://doi.org/10.1029/2019GL086767
Rackauckas, C., & Nie, Q. (2017). DifferentialEquations.jl—A performant and feature-rich ecosystem for solving differential equations in Julia. *Journal of Open Research Software*, *5*(1), 15. https://doi.org/10.5334/jors.151
Rempel, A., & Rice, J. R. (2006). Thermal pressurization and onset of melting in fault zones. *Journal of Geophysical Research*, *111*, B09314. https://doi.org/10.1029/2006jb004314
Rice, J. R. (1973). The initiation and growth of shear bands. In A. C. Palmer (Ed.), *Plasticity and soil mechanics* (p. 263–274): Cambridge University Engineering Department.
Rice, J. R. (1980). The mechanics of earthquake rupture. In A. M. Dziewonski, & E. Boschi (Eds.), *Physics of the earth's interior*. Proc. Intl. School of physics E. Fermi (pp. 555–649). Italian Physical Society/North Holland Publ. Co.
Rice, J. R. (2006). Heating and weakening of faults during earthquake slip. *Journal of Geophysical Research*, *111*, B05311. https://doi.org/10.1029/2005JB004006
Rice, J. R., & Rudnicki, J. W. (1979). Earthquake precursory effects due to pore fluid stabilization of a weakening fault zone. *Journal of Geophysical Research*, *84*(B5), 2177–2193. https://doi.org/10.1029/jb084ib05p02177
Rudnicki, J. W., & Chen, C.-H. (1988). Stabilization of rapid frictional slip on a weakening fault by dilatant hardening. *Journal of Geophysical Research*, *93*, 4745–4757. https://doi.org/10.1029/jb093ib05p04745
Rutter, E. H. (1972). The effects of strain-rate changes on the strength and ductility of Solnhofen limestone at low temperatures and confining pressures. *International Journal of Rock Mechanics and Mining Sciences*, *9*, 183–189. https://doi.org/10.1016/0148-9062(72)90020-4
Samuelson, J., Elsworth, D., & Marone, C. (2009). Shear-induced dilatancy of fluid-saturated faults: Experiment and theory. *Journal of Geophysical Research*, *114*, B12404. https://doi.org/10.1029/2008JB006273
Schmidt, D. A., & Gao, H. (2010). Source parameters and time-dependent slip distributions of slow slip events on the Cascadia subduction zone from 1998 to 2008. *Journal of Geophysical Research*, *115*, B00A18. https://doi.org/10.1029/2008JB006045
Scholz, C. H. (2002). *The mechanics of earthquakes and faulting* (2nd ed.). Cambridge University Press.
Segall, P., & Bradley, A. M. (2012). The role of thermal pressurization and dilatancy in controlling the rate of fault slip. *Journal of Applied Mechanics*, *79*, 031013. https://doi.org/10.1115/1.4005896
Segall, P., & Rice, J. R. (1995). Dilatancy, compaction, and slip instability of a fluid-infiltrated fault. *Journal of Geophysical Research*, *100*(B11), 22155–22171. https://doi.org/10.1029/95jb02403
Segall, P., Rubin, A. M., Bradley, A. M., & Rice, J. R. (2010). Dilatant strengthening as a mechanism for slow slip events. *Journal of Geophysical Research*, *115*, B12305. https://doi.org/10.1029/2010JB007449
Sibson, R. H., & Toy, V. G. (2006). The habitat of fault-generated pseudotachylyte: Presence vs. absence of friction melt. In R. Abercrombie, A. McGarr, G. Di Toro, & H. Kanamori (Eds.), *Earthquakes: Radiated energy and the physics of faulting, Geophys. Monogr. Ser*. (Vol. *170*, pp. 153–166): American Geophysical Union. https://doi.org/10.1029/170gm16
Sleep, N. H. (2006). Frictional dilatancy. *Geochemistry, Geophysics, Geosystems*, *7*(10), Q10008. https://doi.org/10.1029/2006GC001374
Suzuki, T., & Yamashita, T. (2007). Understanding of slip-weakening and -strengthening in a single framework of modeling and its seismological implications. *Geophysical Research Letters*, *34*, L13303. https://doi.org/10.1029/2007GL030260
Suzuki, T., & Yamashita, T. (2008). Nonlinear effects of temperature, fluid pressure, and inelastic porosity on dynamic fault slip and fault tip propagation: Emergence of slip strengthening and pulse-like fault slip. *Journal of Geophysical Research*, *113*, B07304. https://doi.org/10.1029/2008JB005581
Suzuki, T., & Yamashita, T. (2009). Dynamic modeling of slow earthquakes based on thermoporoelastic effects and inelastic generation of pores. *Journal of Geophysical Research*, *114*, B00A04. https://doi.org/10.1029/2008JB006042
Teufel, L. W. (1981). Pore volume changes during frictional sliding of simulated faults. In N. L. Carter, M. Friedman, J. M. Logan, & D. W. Stearns (Eds.), *Mechanical behavior of crustal rocks: The handin volume*. Geophys. Monogr. Ser (p. 135–145). American Geophysical Union.
Viesca, R. C., & Garagash, D. I. (2015). Ubiquitous weakening of faults due to thermal pressurization. *Nature Geoscience*, *8*, 875–879. https://doi.org/10.1038/ngeo2554

Viesca, R. C., & Garagash, D. I. (2018). Numerical methods for coupled fracture problems. *Journal of the Mechanics and Physics of Solids*, *113*, 13–34. https://doi.org/10.1016/j.jmps.2018.01.008

Weng, H. (2021). Slow slip events are regular earthquakes. preprint available at Research Square. https://doi.org/10.21203/rs.3.rs-448196/v1

Weng, H., & Ampuero, J.-P. (2019). The dynamics of elongated earthquake ruptures. *Journal of Geophysical Research*, *124*, 8584–8610. https://doi.org/10.1029/2019JB017684

Wibberley, C. A. J., & Shimamoto, T. (2003). Internal structure and permeability of major-lip fault zones: The Median Tectonic Line in Mie Prefecture, southwest Japan. *Journal of Structural Geology*, *25*, 59–78. https://doi.org/10.1016/s0191-8141(02)00014-7

Wong, T.-F. (1982). Shear fracture energy of Westerly granite from post-failure behavior. *Journal of Geophysical Research*, *87*(B2), 990–1000. https://doi.org/10.1029/jb087ib02p00990